

Flow Near the Contact Line of an Evaporating Droplet

Master thesis

Oscar Bloemen

Graduation committee

Prof. dr. D. Lohse

Dr. J.H. Snoeijer

Dr. H.T.M. van den Ende

H. Gelderblom, MSc

*Physics of Fluids group, Faculty of Science and Technology,
University of Twente, 7500 AE Enschede, The Netherlands*

January 13, 2012

Abstract

Evaporating droplets with small contact angles possess an evaporative flux that is singular at the contact line. It has been argued that near the contact line this singularity gives such a powerful outflow, that the flow must be normal to the surface of the droplet. A flow field with this property prohibits application of the lubrication theory near the contact line of the droplet. In this work the flow field near the contact line is solved analytically for an arbitrary contact angle. From this solution we demonstrate that the lubrication approximation does accurately describe the flow field near the contact line, which is in agreement with experiments. The analytical solution of the flow field near the contact line also gives the opportunity to observe the flow for larger contact angles. Remarkably, for these contact angles, regions are found where the flow is in the opposite direction as one might expect. To investigate these regions in the whole droplet, numerical simulations are performed. The simulations confirm existence of these regions near the contact line, away from the contact line we see that these regions correspond to a flow circulation in the droplet.

Contents

1	Introduction	1
1.1	Evaporating droplets	1
1.2	Scope of this work	3
2	Background theory	5
2.1	Evaporative flux	5
2.1.1	Fitting the wedge solution to the solution for the entire droplet	7
2.1.2	Changing contact angle due to mass outflow	8
2.2	Internal flow	9
2.2.1	Height-averaged flow	9
2.2.2	Lubrication Approximation	11
3	Stokes flow in a wedge	13
3.1	Problem description	13
3.2	Flow due to evaporation	15
3.3	Flow due to the moving interface	16
4	Analytical results	17
4.1	Wedge flow fields	17
4.2	Regions of reversed flow	20
4.2.1	Separatrices in the flow due to evaporation	20
4.2.2	Separatrices in the flow due to the moving interface	22
4.3	Dominant flow driving mechanism	22
4.4	Towards the lubrication approximation	23
4.4.1	Why the lubrication theory works	24
5	Wedge flow simulation	27
5.1	Wedge model description	27
5.2	Set-up in COMSOL	28
5.3	Results for $\theta = 40^\circ$	29
5.4	Results for $\theta = 130^\circ$	32
6	Numerical results	33
6.1	Droplet model description	33
6.2	Results	35
6.2.1	Concentration field and evaporative flux	36
6.2.2	Droplet flow fields	37
7	Discussion and conclusion	41
7.1	Conclusion	41
7.2	Discussion and recommendations for future research	42
	Acknowledgments	43

Bibliography	44
List of Figures	47
A Typical droplet properties	49

Chapter 1

Introduction

1.1 Evaporating droplets

The characteristic shape of a coffee stain, a dark ring of particles close to the perimeter, can be observed in our daily life, see figure 1.1. The ring-like residue left on the substrate is evidence of a, perhaps spilled, colloidal droplet which has dried over time. The formation of deposit close to the perimeter is called the coffee stain effect, but it is not unique for coffee droplets and is shared among evaporating colloidal droplets in general. The pattern formation by drying colloids has many applications related to self-assembly [1], e.g. in the fields of colloidal crystal generation where crystals can be grown layer-by-layer [2], crystals with evenly spaced cracks from the capillary forces [3], and self-assembling nano-structures by fast evaporation and particle attraction to the air [4]. The effect can also be disadvantageous if a homogeneous coating is needed, for example in the inkjet printing industry [5, 6] or in DNA analysis [7, 8], where the clustering of DNA around the perimeter makes it impossible to examine the samples.

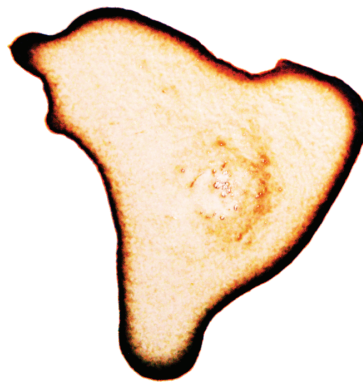


Figure 1.1: A typical coffee stain.

For applications, better understanding of the coffee stain effect is the key for improving control over the deposition of particles. When fluid evaporates from the droplet, the volume decreases and the droplet will shrink as seen figure 1.2 (a) and (b). However, if the contact line is pinned (remains at the same position) the fluid at the contact line has to be replenished with fluid from inside the droplet and an internal flow towards the contact line must exist, see figure 1.2 [5]. The particles inside the fluid are then transported by this flow to the contact line, resulting in the distinctive pattern. For this pattern to appear it is thus necessary to have a pinned, or slowly moving, contact line during evaporation of the droplet. This pinned contact line can occur for various reasons, e.g. roughness of the substrate or self-pinning by the accumulated particles at the contact line [9].

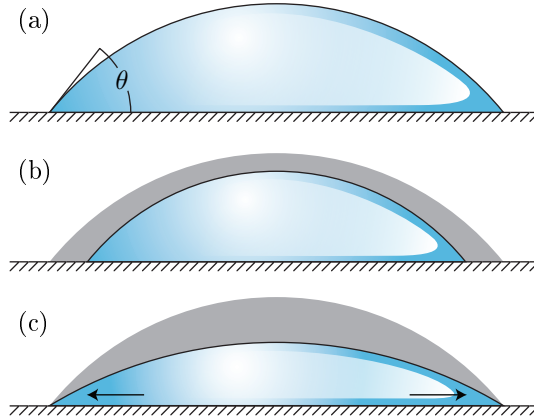


Figure 1.2: Illustration of the origin of flow towards the contact line. (a) The initial droplet of contact angle θ (b) Partially evaporated droplet with moving contact line. (c) Partially evaporated droplet with pinned contact line, the arrows represent the direction of the flow inside the droplet.

In order to describe the flow inside the droplet, the mass outflow due to evaporation has to be known. The evaporative flux close to the contact line was expressed by Deegan et al. [5] while the evaporative flux over the entire droplet was given by Popov [10]. During evaporation, the fluid from the droplet vaporizes which gives a saturated vapor concentration around the free surface. If the ambient air is not saturated with vapor, the vapor will then diffuse outward [5], giving a mass flux normal to the free surface of the droplet. Gelderblom et al. [11] showed that this diffusion model accurately describes the evaporation process by comparing experimental data of the rate of mass loss of the droplet with the analytical solution of the diffusion model, see figure 1.3. Interestingly, the evaporative flux is strongest, and even diverges, near the contact line due to the singular geometry of the droplet, see the pointy shape of the droplet in figure 1.4. This singularity in the evaporative flux gives rise to a singular velocity field [5, 12] and will present problems in finding analytical and numerical solutions of the velocity field [13, 14, 15].

A height-averaged velocity was derived from a mass balance in the droplet by Deegan et

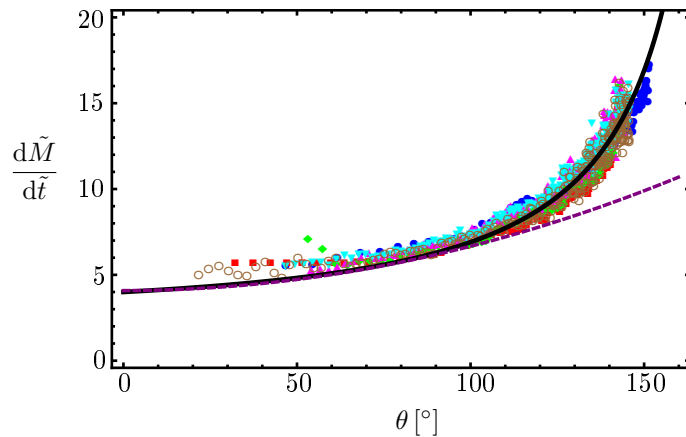


Figure 1.3: The rate of mass loss of the droplet versus contact angle for different initial droplet volumes from experiments (various markers and colors). Predictions from the Popov model [10] (black solid line) and the model of Hu and Larson (purple dashed line) for contact angles smaller than 90° [16]. Reprinted from [11]

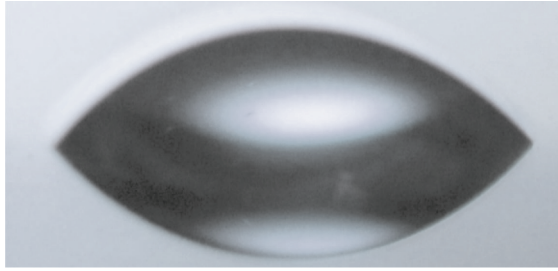


Figure 1.4: A droplet with reflection on the substrate. Close to the contact line the sharp edge of the singular geometry is seen.

al. [5]. For small contact angles, the radius of the droplet becomes large compared to the height of the droplet and the lubrication approximation can be used to obtain a velocity profile for the internal flow from this height averaged velocity [1]. However, it is argued that this theory does not hold close to the contact line due to the singular evaporative flux. Hu & Larson [16] state that because of the singular evaporative flux for small contact angles, the velocity close to the contact line must be approximately normal to the free surface, see figure 1.5. If this is indeed the case, this should be accounted for in the approximation whereas the vertical velocity is normally neglected. Experimental data however, agrees well with velocity profiles obtained directly from the lubrication approximation [1]. This contradiction immediately brings a question to mind: why does the lubrication approximation correctly predicts the flow behavior close to the contact line for small contact angles, even though the evaporative flux is singular at the contact line? To answer this question, the exact solution of the flow field close to the contact line has to be known, which is what we will derive in this thesis.

1.2 Scope of this work

In this thesis we consider small droplets (radius of order 10^{-3} m) with the same properties as in the experiment performed by Marín et al. [1]¹. The influence of gravity on droplets of this size is negligible (Bond number of order 10^{-1}), which results in droplets shaped as spherical caps. For analysis of the argument of Hu & Larson, we are mainly interested in the region close to the contact line. Here, both the curvature of the free surface and the contact line vanish and the geometry can be approximated as a two-dimensional wedge.

The general problem of an evaporating droplet consists of a vapor concentration outside the droplet from which an evaporative flux is found that drives the internal flow, see figure 1.6. Using the evaporative flux for the wedge, we will solve for the flow field in the droplet. From experimental

¹For convenience, the properties of the droplet are listed in appendix A.

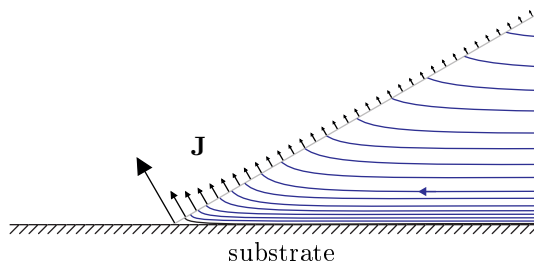


Figure 1.5: Visualization of the concept of Hu & Larson [17]. Sketched streamlines are going to the normal of the free surface due to the high evaporative flux at the contact line. In this thesis we will verify this hypothesis by computing the streamlines.

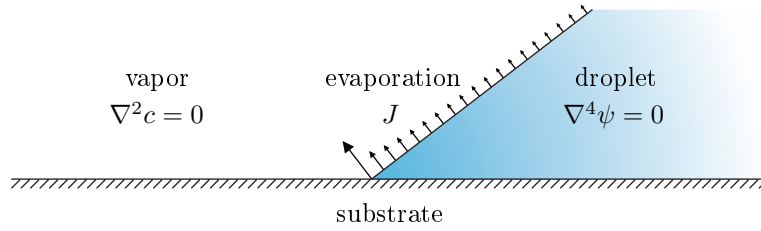


Figure 1.6: Schematic representation of the problem in the wedge where c is the vapor concentration, J the evaporative flux, and ψ the stream function. Outside the wedge, the concentration field of the liquid has to be solved with the Laplace equation to find the evaporative flux. Inside the wedge the flow-field of the liquid can be found by solving the biharmonic equation.

data [1], we find that the velocity is of order $\mu m/s$ ($Re = 10^{-3}$) [1]. In this low-Reynolds regime we will search for a stream function that satisfies the Stokes equations to find the velocity field in the wedge. Expansions of this analytic solution for the flow field for small contact angles will be used to verify the lubrication solution.

Remarkably, regions are found where the flow is in opposite direction as one expects. When there is an outflux at the boundary, one might expect an internal flow to this boundary to replenish the fluid. From the analytical wedge flow solution, contact angle regimes are found where the flow is directed towards the center of the droplet. We will describe some characteristics of these regimes from the analytical solution. We wonder if these regimes can also be seen in the geometry of the whole droplet, and, if they are seen, what they will look like. To address this question, we will perform numerical simulations that give the full flow profile in the entire droplet. The concentration field and internal flow field are linked by the evaporative flux and solved in COMSOL². The wedge geometry is used as validation case, and shows good agreement with the analytic results. A set-up is made for the whole droplet geometry, from where circulations in the droplet are seen, but limited time restricted us from performing calculations in detail.

In chapter 2, we describe the relevant literature. First we describe the solution for evaporative flux close to the contact line. From the evaporative flux, the rate of mass loss for the whole droplet is calculated, giving an expression contact angle change in time. Next, a height-averaged expression of the internal flow will be given from a mass balance, from which the flow field is calculated using the lubrication approximation.

In chapter 3 we derive an analytical expression for the flow close to the contact line. Here, the Stokes equations are solved in the wedge, where we use the expressions for the evaporative flux and changing contact angle as kinematic boundary conditions. In chapter 4 we discuss our findings from the analytical solution. We show the flow fields for various contact angles, and continue with a description of the regions with reversed flow. From here, we close the analytical research with a discussion on the validity of the lubrication approximation close to the contact line.

In chapter 5 we describe the simulation set-up for the validation case and present the results. In chapter 6 the set-up of the numerical simulation for the entire droplet is discussed after which we show the results of this simulation and make a comparison with the analytical wedge solution. We will finish the thesis in chapter 7 with a general discussion of the work and a listing of all our findings.

²COMSOL MULTIPHYSICS®, version 4.2.1.110.

Chapter 2

Background theory

In this chapter we will derive an expression for the evaporative flux in the vicinity of the contact line. This flux will be used to calculate the moving free surface of the evaporating droplet. Both equations are then used to define the local rate of mass loss of the droplet. We derive the height-averaged velocity, which we will use in the lubrication approximation to find the flow field in the entire droplet.

2.1 Evaporative flux

The evaporation time of the droplet (order 10^3 s) is slow compared to the time that it takes to build up the concentration field around the droplet (order 10^{-2} s). Fluid from the droplet has to transfer from the droplet towards the air surrounding the droplet, thereby crossing the interface. This transfer rate is characterized by a time scale of order 10^{-10} s. The time it would take for diffusion to build up a profile around the droplet is of order R^2/D_{va} which is about 10^{-2} s [18]. Hence, the problem is quasi-steady and the rate limiting step is given by the diffusion time of the vapor in air. Fick's second law can be used to find the concentration field c ;

$$\frac{\partial c}{\partial t} = D_{va} \nabla^2 c, \quad (2.1)$$

where D_{va} is the diffusion constant for vapor in air and t is time.

From here, the evaporative flux \mathbf{J} can be found by Fick's law,

$$\mathbf{J} = -D_{va} \nabla c. \quad (2.2)$$

We will solve these equations in the vicinity of the contact line for the wedge geometry. Polar coordinates ρ and ϕ are introduced with the origin coinciding with the contact line. The free surface of the droplet is located at $\phi = 0$, see figure 2.1. We introduce a non-dimensional length $\tilde{\rho}$, and concentration \tilde{c} , and we define a characteristic velocity U (of order μ^m/s),

$$\tilde{\rho} = \frac{\rho}{R}, \quad (2.3)$$

$$\tilde{c} = \frac{c - c_\infty}{\Delta c}, \text{ and} \quad (2.4)$$

$$U = \frac{D_{va} \Delta c}{\rho_l R}, \quad (2.5)$$

where R is the radius of the contact line, c_∞ the concentration far away from the droplet, $\Delta c = c_s - c_\infty$, and ρ_l the density of the fluid. Substitution of these quantities into (2.2) and (2.1) and

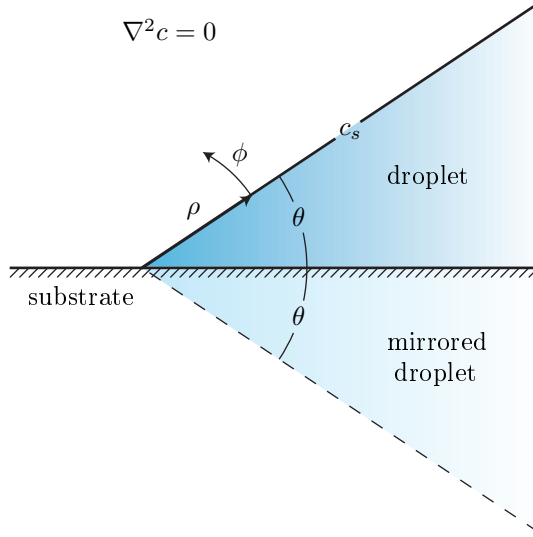


Figure 2.1: Wedge-shaped geometry close to the contact line. The droplet is mirrored with respect to the substrate. Polar coordinates ρ and ϕ are indicated as well as the contact angle θ .

discarding the temporal derivative because of the quasi-steady problem leads to, after dropping the tildes,

$$\frac{1}{\rho t} \mathbf{J} = -U \left(\frac{\partial c}{\partial \rho} \mathbf{e}_\rho + \frac{1}{\rho} \frac{\partial c}{\partial \phi} \mathbf{e}_\phi \right), \text{ and} \quad (2.6)$$

$$0 = \frac{1}{\rho} \frac{\partial}{\partial \rho} \left(\rho \frac{\partial c}{\partial \rho} \right) + \frac{1}{\rho^2} \frac{\partial^2 c}{\partial \phi^2}, \quad (2.7)$$

where \mathbf{e}_ρ and \mathbf{e}_ϕ are the unit vectors in radial and angular direction respectively.

The substrate imposes an impermeability boundary condition for the flux \mathbf{J} . This zero-flux boundary condition can be satisfied mathematically, but here it is handled by mirroring the problem with respect to the substrate, thereby automatically satisfying impermeability, see figure 2.1. The mirrored free surface is located at $\phi = 2(\pi - \theta)$.

For simplicity, it is chosen to solve for $c' = c - 1$ which results in homogeneous boundary conditions at the free surface and mirrored free surface,

$$c'(\rho, \phi) = 0 \text{ at } \phi = 0 \vee 2(\pi - \theta). \quad (2.8)$$

The Laplace equation is solved with separation of variables. Substitution of $c' = P(\rho)\Phi(\phi)$ leads to

$$\rho \frac{1}{P(\rho)} \frac{\partial}{\partial \rho} \left(\rho \frac{\partial}{\partial \rho} P(\rho) \right) = \lambda^2 = -\frac{1}{\Phi(\phi)} \frac{\partial^2}{\partial \phi^2} \Phi(\phi).$$

where λ is a constant. Here, the left hand side is an Euler equation and has as solution

$$P(\rho) = C_1 \rho^\lambda + C_2 \rho^{-\lambda} \text{ for } \lambda > 0 \text{ and } \rho > 0.$$

For $\lambda = 0$, a solution is lost and reduction of order has to be used to find a second solution [19],

$$P(\rho) = C_1 + C_2 \ln \rho \text{ for } \lambda = 0 \text{ and } \rho > 0.$$

Solving the right hand side of (2.1) results in

$$\begin{aligned} \Phi(\phi) &= C_3 \cos \lambda \phi + C_4 \sin \lambda \phi \text{ for } \lambda > 0, \text{ and} \\ \Phi(\phi) &= C_3 \phi + C_4 \text{ for } \lambda = 0. \end{aligned}$$

Combined, the general solution to the Laplace equation in polar coordinates reads

$$c'(\rho, \phi) = C_{1,0} + C_{2,0} \ln \rho + C_{3,0} \phi + C_{4,0} \phi \ln \rho + \sum_{n=1} (C_{1,n} \rho^{\lambda_n} + C_{2,n} \rho^{-\lambda_n}) (C_{3,n} \cos \lambda_n \phi + C_{4,n} \sin \lambda_n \phi).$$

Since the current problem will only be valid locally near the contact line, the logarithmic and $\rho^{-\lambda}$ terms have to be removed as they will result in an unphysical concentration at the origin;

$$c'(\rho, \phi) = C_{1,0} + C_{3,0} \phi + \sum_{n=1} \rho^{\lambda_n} (C_{3,n} \cos \lambda_n \phi + C_{4,n} \sin \lambda_n \phi).$$

In order to satisfy the homogeneous boundary condition at the free surface ($\phi = 0$), all $C_{3,n}$ terms have to be zero. From the homogeneous boundary condition at $\phi = 2(\pi - \theta)$, an expression for λ is found,

$$\lambda = \frac{\pi}{2(\pi - \theta)} n \text{ with } n \in \mathbb{N}. \quad (2.9)$$

Hence, for the concentration field close to the contact line we find

$$c(\rho, \phi) = c_s + \sum_{n=1} \rho^{\lambda_n} \sin \lambda_n \phi. \quad (2.10)$$

Now (2.6) can be used to calculate the evaporative flux at the free surface,

$$\frac{J}{\rho_l} = -U \sum_{n=1} C_n \lambda_n \rho^{\lambda_n - 1}. \quad (2.11)$$

Close to the contact line the first term is dominant, hence

$$\frac{J}{\rho_l} = -A(\theta) U \rho^{\lambda - 1}, \quad (2.12)$$

where prefactor $A(\theta)$ is found from the full spherical-cap solution [10]. Contours of the concentration field together with the evaporative flux are shown in figure 2.2.

2.1.1 Fitting the wedge solution to the solution for the entire droplet

The prefactor $A(\theta)$ is the link between the local wedge approximation and the global problem of the evaporating droplet. $A(\theta)$ has to be fitted such that the wedge solution matches with the solution for the entire droplet, available from Popov [10].

For small contact angles λ can be approximated as $1/2$ and the exact solution of a disc-like droplet can be used [10],

$$\frac{J_{\text{disc}}}{\rho_l} = \frac{2}{\pi} \frac{U R}{\sqrt{R^2 - r^2}}, \quad (2.13)$$

where r is the radius from the center of the droplet, i.e.

$$\rho = 1 - \frac{r}{R}.$$

This flux can be approximated for small ρ ,

$$\frac{J_{\text{disc}}}{\rho_l} = \frac{\sqrt{2} U}{\pi} \frac{1}{\sqrt{\rho}},$$

from which follows, for small ρ and small contact angles,

$$A \simeq \frac{\sqrt{2}}{\pi}. \quad (2.14)$$

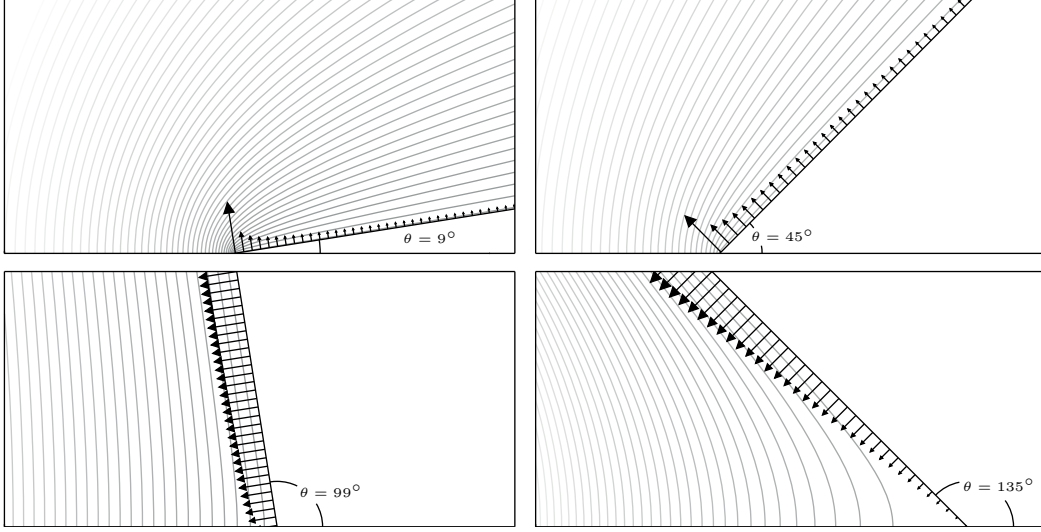


Figure 2.2: Contours of constant vapor concentration and corresponding evaporative flux at the free surface, (2.12), for different contact angles. Note that the solution is scale independent and therefore no axis scaling is shown.

2.1.2 Changing contact angle due to mass outflow

Now the evaporative flux is known, we can calculate the rate of mass loss of the droplet. Since the droplet is described by a spherical cap with a pinned radius, we can relate the rate of mass loss to a contact angle change.

Evaporation gives a total mass outflow,

$$\frac{\partial M}{\partial t} = \int_S J(\rho) dS, \quad (2.15)$$

where M is the mass of the droplet and S is the free surface of the droplet. This outflow has to equal the mass change of the evaporating droplet,

$$\frac{\partial M}{\partial t} = \rho_l \frac{\partial V}{\partial \theta} \frac{d\theta}{dt}, \quad (2.16)$$

where V is the volume of the droplet.

In the limit of small contact angles the steps of (2.15) and (2.16) can be approximated. Starting with the evaporating mass, using (2.13), we find

$$\frac{dM}{dt} = \int_0^R 4U \rho_l \frac{Rr}{\sqrt{R^2 - r^2}} dr = 4U \rho_l R^2. \quad (2.17)$$

For small contact angles, we can approximate the droplet shape by a parabola,

$$h(r, t) = \frac{R^2 - r^2}{2R},$$

where h is the height of the droplet, from which the volume is found to be

$$V = 2\pi \int_0^R h(r, t) r dr = \frac{\pi}{4} R^3 \theta. \quad (2.18)$$

The volume can now be substituted into (2.16), giving

$$\frac{\partial M}{\partial t} = \frac{\pi}{4} \rho_l R^3 \frac{\partial \theta}{\partial t}. \quad (2.19)$$

By equating (2.17) to (2.19), we find the rate of contact angle change

$$\frac{d\theta}{dt} = -\frac{16 U}{\pi R}. \quad (2.20)$$

Likewise, for the full spherical cap of arbitrary contact angle we can write

$$\frac{d\theta}{dt} = \frac{1}{\rho_l} \frac{\partial \theta}{\partial V} \int_S J(\rho) dS.$$

Using the evaporative flux for the whole droplet, one finds

$$\frac{d\theta}{dt} = -B(\theta) \frac{U}{R} \quad (2.21)$$

where $B(\theta)$ is of order unity and can be found from (A8) in [10].

2.2 Internal flow

The evaporative flux drives a flow inside the droplet. First we derive the height-averaged velocity from the evaporative flux, then we show how the lubrication approximation can be used to find an expression for the entire flow field.

2.2.1 Height-averaged flow

The flow inside the droplet can be described in a height-averaged way. A mass balance is evaluated over an annulus of an infinitesimal ring width dr . The axis of the annulus coincides with the axis of symmetry of the droplet, see figure 2.3.

The change of mass for the annulus at r can be described as

$$\underbrace{\frac{\partial}{\partial t} m}_{\text{rate of mass loss}} = \underbrace{Q_{\text{in}} - Q_{\text{out}}}_{\text{change due to mass flux}} - \underbrace{Q_J}_{\text{change due to evaporation}}, \quad (2.22)$$

where t is the time, m the mass of the fluid ring, $Q_{\text{in/out}}$ the mass flux in and out at r due to convection, and Q_J the mass flux due to evaporation at r .

The mass of the annulus at r can be expressed as

$$m = 2\pi r dr h \rho_l,$$

where h is the droplet height at r and ρ_l the density of the liquid. The only time-dependent variable is the droplet height. Hence, the rate of mass loss at r equals

$$\frac{\partial}{\partial t} m = 2\pi r dr \rho_l \frac{\partial}{\partial t} h. \quad (2.23)$$

Convection of fluid inside the droplet contributes a mass flux in and out of the fluid ring. The mass flux in the ring is given by

$$Q(r) = 2\pi r h(r) \bar{u}_r(r) \rho_l, \quad (2.24)$$

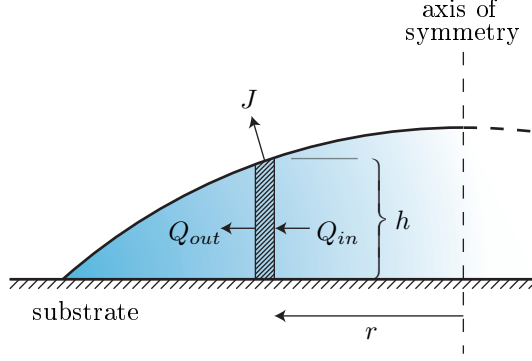


Figure 2.3: Schematic drawing of the cross section of an axisymmetric droplet on a substrate. An annulus of width dr in the droplet at radius r with height h is shaded. The different in- and outflows of mass in the annulus are visualized as Q , where the subscripts *in* and *out* denote the mass flux by convection, and J , which is the mass flux by evaporation.

where $Q(r)$ is the mass flux due to convection at r , and \bar{u}_r the height-averaged radial velocity. For the annulus, the net rate of mass loss due to convection is

$$Q_{in} - Q_{out} = Q(r) - Q(r + dr) = -2\pi dr \frac{\partial}{\partial r} Q(r). \quad (2.25)$$

Now the remaining term in (2.22) is the mass flux due to evaporation. Multiplying the evaporative flux with the area of the annulus at the free surface yields

$$Q_J = 2\pi r dr J(r, t) \sqrt{1 + \left(\frac{\partial h}{\partial r}\right)^2}. \quad (2.26)$$

Combination of (2.22), (2.23), (2.25) and (2.26) results in

$$\rho_l \frac{\partial h}{\partial t} = -\frac{1}{r} \frac{\partial}{\partial r} Q(r) - J(r, t) \sqrt{1 + \left(\frac{\partial h}{\partial r}\right)^2}. \quad (2.27)$$

For small contact angles, the spatial derivative of h will be small compared to unity and can be neglected. This approximation leads to the following equation:

$$\rho_l \frac{\partial h}{\partial t} = -\frac{1}{r} \frac{\partial}{\partial r} Q(r) - J(r, t). \quad (2.28)$$

The height-averaged velocity for small contact angles, close to the contact line, can be calculated from (2.28) [1]. Substitution of the relations (2.13) and (2.20) into (2.28) gives

$$\frac{1}{\rho_l} \frac{\partial Q_r}{\partial r} = \frac{2}{\pi} \frac{U R r}{\sqrt{R^2 - r^2}} - \frac{16 U (R^2 - r^2) r}{\pi R 2R}. \quad (2.29)$$

Integration now gives the height-averaged velocity by using (2.24),

$$\bar{u}_r = \frac{Q_r}{r h} = \frac{2U}{\pi r h} \left(R \sqrt{R^2 - r^2} - \frac{(R^2 - r^2)^2}{R^2} \right). \quad (2.30)$$

In the vicinity of the contact line, a similar expansion can be applied as was done in section 2.1.1. Neglecting the higher order terms yields

$$\bar{u}_r = \frac{Q_r}{\rho_l r h} = \frac{2\sqrt{2} U R}{\pi h} \sqrt{\rho}. \quad (2.31)$$

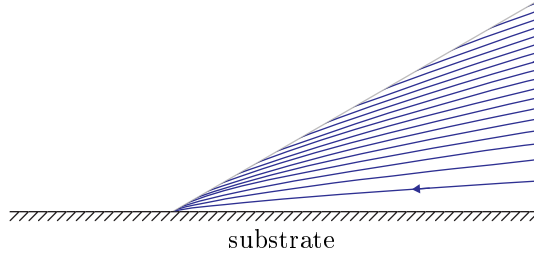


Figure 2.4: Streamlines of the flow approximated with the lubrication approximation, (2.33) and (2.34), in the wedge with $\theta = 30^\circ$.

2.2.2 Lubrication Approximation

An estimate of the full velocity field can be obtained from the height-averaged velocity. For small contact angles, the height of the droplet is small compared to the radius. Because of these length scales, we estimate that variations along the free surface of the droplet are much more gradual than the variations normal to the free surface of the droplet [20]. In the introduction it is explained that there must exist a viscous flow to the contact line, and using the lubrication approximation, we can write for this flow

$$\frac{\partial p}{\partial r} = \mu \frac{\partial^2 u_r}{\partial z^2}, \quad (2.32)$$

Where p is the pressure, μ the dynamic viscosity, and u_r the radial velocity. At the substrate a no-slip boundary condition is imposed,

$$u_r|_{z=0} = 0.$$

At the free surface there is no force acting tangential to the fluid, and therefore no-shear stress is implied,

$$\left[\frac{\partial u_r}{\partial z} + \frac{\partial u_z}{\partial r} \right]_{z=h} = 0,$$

where the second term on the of the left hand side is neglected in the lubrication approximation. When using these boundary conditions, integration of (2.32) gives the radial velocity,

$$u_r = \frac{1}{\mu} \frac{\partial p}{\partial r} \left(\frac{1}{2} z^2 - hz \right).$$

This profile can be expressed in terms of the height-averaged velocity, (2.31),

$$\bar{u}_r = -\frac{1}{3\mu} \frac{\partial p}{\partial r} h^2 = \frac{2\sqrt{2}U R}{\pi} \frac{R}{h} \sqrt{\rho},$$

to give an expression for the radial velocity [1];

$$u_r = -\frac{6\sqrt{2}U R}{\pi} \frac{R}{h} \sqrt{\rho} \left[\frac{1}{2} \left(\frac{z}{h} \right)^2 - \frac{z}{h} \right]. \quad (2.33)$$

From the continuity equation we can find an expression for the vertical velocity

$$u_z = \frac{2\sqrt{2}U}{\pi} \left[\frac{5}{2} \left(\frac{z}{h} \right)^3 - \frac{9}{2} \left(\frac{z}{h} \right)^2 \right]. \quad (2.34)$$

The streamlines given by this velocity field are displayed in figure 2.4.

Hu & Larson [17] argue that the lubrication approximation is not applicable close to the contact line. For small contact angles, the evaporative flux is almost vertical, and the vertical velocity can be approximated as:

$$u_z \approx \frac{\partial h}{\partial t} + \frac{J}{\rho l}.$$

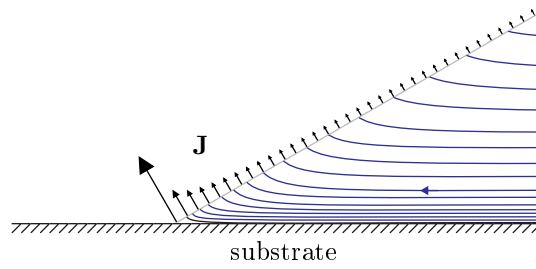


Figure 2.5: Visualization of the concept of Hu & Larson [17]. Sketched streamlines going to the normal of the free surface due to the high evaporative flux at the contact line.

Close to the contact line, they state that this term becomes significant due to the singularity in the evaporative flux and cannot be neglected as is done in the lubrication approximation; see figure 2.5 for an impression.

Experiments [1], however, do show good agreement with the lubrication approximation close to the contact line. To understand why, we will solve the velocity field in the wedge in full detail.

Chapter 3

Stokes flow in a wedge

The flow field inside a wedge will be solved by finding a stream function. We will start by finding a general solution for the biharmonic equation in the wedge which describes the Stokes flow field. At the free surface we will impose a no-shear condition and a flow due to evaporation and due to the interface movement.

3.1 Problem description

Because the flow inside the droplet is given by the Stokes equations, the flow field inside the wedge can be described by a stream function ψ , which has to satisfy the biharmonic equation,

$$\nabla^4 \psi = 0. \quad (3.1)$$

Polar coordinates ρ and ϕ with origin at the contact line will again be a convenient choice to describe the problem. This time, however, $\phi = 0$ coincides with the substrate and $\phi = \theta$ with the free surface, see figure 3.1. Given the coordinate system, the radial and angular velocity components can be expressed respectively as

$$u_\rho = \frac{1}{\rho} \frac{\partial \psi}{\partial \phi} \quad \text{and} \quad u_\phi = -\frac{\partial \psi}{\partial \rho}, \quad (3.2)$$

and the boundary conditions can be specified in terms of the stream function:

1. No-slip at the substrate,

$$u_\rho|_{\phi=0} = \frac{1}{\rho} \frac{\partial \psi}{\partial \phi} \Big|_{\phi=0} = 0. \quad (3.3)$$

2. Impermeability of the substrate,

$$u_\phi|_{\phi=0} = \frac{\partial \psi}{\partial \rho} \Big|_{\phi=0} = 0. \quad (3.4)$$

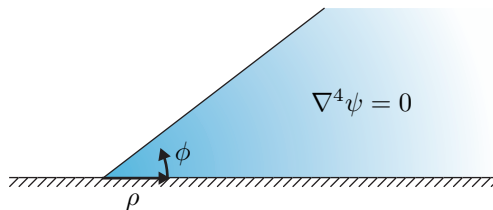


Figure 3.1: Stokes flow problem in the wedge with polar coordinates ρ and ϕ and the origin located at the contact line. The biharmonic equation is solved in the shaded area with the boundary conditions (3.3), (3.4), (3.5), and (3.6).

3. Similar as in section 2.2.2, here to a no-shear stress condition is imposed at the free surface,

$$\mu \left[\rho \frac{\partial}{\partial \rho} \left(\frac{1}{\rho} u_\phi \right) + \frac{1}{\rho} \frac{\partial}{\partial \phi} u_\rho \right]_{\phi=\theta} = \left[\frac{1}{\rho^2} \frac{\partial^2}{\partial \phi^2} \psi - \rho \frac{\partial}{\partial \rho} \left(\frac{1}{\rho} \frac{\partial}{\partial \rho} \psi \right) \right]_{\phi=\theta} = 0. \quad (3.5)$$

4. We impose an outflow due to the evaporation at the free surface. In addition, there is a movement due to the decreasing volume of the droplet. In the wedge approximation this can be visualized as a closing hinge. Hence, the kinematic boundary condition at the free surface reads

$$u_\phi|_{\phi=\theta} = - \frac{\partial \psi}{\partial \rho} \Big|_{\phi=\theta} = \rho \frac{d\theta}{dt} - \frac{1}{\rho l} J(\rho).$$

Substitution of (2.21) and (2.12) shows that both conditions give power laws in ρ ,

$$- \frac{\partial \psi}{\partial \rho} \Big|_{\phi=\theta} = -\rho B(\theta) \frac{U}{R} + A(\theta) U \rho^{\lambda-1}, \quad (3.6)$$

where

$$\lambda = \frac{\pi}{2(\pi - \theta)} \quad (3.7)$$

as in (2.9) with $n = 1$.

Since the biharmonic equation is similar to applying the Laplacian twice, again separation of variables is chosen to handle this problem. Substitution of

$$\psi(\rho, \phi) = P(\rho) \Phi(\phi),$$

into (3.1) results in

$$P_{\rho\rho\rho\rho} \Phi + \frac{2}{\rho} P_{\rho\rho\rho} \Phi + \frac{1}{\rho^2} P_{\rho\rho} (2\Phi_{\phi\phi} - \Phi) + \frac{1}{\rho^3} P_\rho (\Phi - 2\Phi_{\phi\phi}) + \frac{1}{\rho^4} P (\Phi_{\phi\phi\phi\phi} + 4\Phi_{\phi\phi}) = 0, \quad (3.8)$$

where the subscripts denote the derivatives, e.g. $P_\rho = \partial P / \partial \rho$. Using our experience from the Laplace equation for the concentration field c , section 2.1, a power law for $P(\rho)$ and a harmonic function for $\Phi(\phi)$ are tried,

$$P(\rho) = C_1 \rho^\alpha \text{ and } \Phi(\phi) = C_2 \cos \beta \phi + C_3 \sin \beta \phi.$$

When inserting these into (3.8), a relation for β in terms of α is found;

$$\beta = \alpha - 2, -\alpha, +\alpha, \text{ and } -\alpha + 2.$$

The linear independent solutions can now be inserted into (3.1) to find the general solution to the biharmonic equation,

$$\psi = \rho^\alpha (C_1 \cos \alpha \phi + C_2 \sin \alpha \phi + C_3 \cos(\alpha - 2) \phi + C_4 \sin(\alpha - 2) \phi) \text{ for } \alpha \neq 0, 1, 2. \quad (3.9)$$

For the special cases $\alpha = 1$ or 2 ,¹ linearly independent solutions are lost and the general solution degenerates to [21, 22]

$$\psi = \rho (C_1 \cos \phi + C_2 \sin \phi + C_3 \phi \sin \phi + C_4 \phi \cos \phi) \quad (3.10)$$

for $\alpha = 1$, and

$$\psi = \rho^2 (C_1 \cos 2\phi + C_2 \sin 2\phi + C_3 + C_4 \phi) \quad (3.11)$$

for $\alpha = 2$. All that now remains to obtain the flow field is to find the coefficients C_1 to C_4 from the boundary conditions.

The kinematic boundary condition (3.6) introduces two powers of ρ that will, in general, not be equal. This means that for each power of ρ , (3.9) has to be solved independently, giving a solution of the flow due to the moving interface and a flow due to evaporation. Superposition of both solutions will then give the complete flow field in the wedge.

¹The special case of $\alpha = 0$ will not be used.

3.2 Flow due to evaporation

The flow field in the wedge due to evaporative flux is solved first. The kinematic boundary condition is expressed as:

$$\left. \frac{\partial \psi}{\partial \rho} \right|_{\phi=\theta} = \alpha \rho^{\alpha-1}(\dots) = A(\theta) U \rho^{\lambda-1}$$

and hence,

$$\alpha = \lambda. \quad (3.12)$$

First a solution is sought for $\lambda \neq 1$ or 2 . To find C_1 to C_4 we use the boundary conditions from the previous section and (3.2). Starting with no-slip, (3.3), we find

$$C_4 = -\frac{\lambda}{\lambda-2} C_2.$$

Impermeability, (3.4), gives

$$C_3 = -C_1. \quad (3.13)$$

These relations are now substituted into the no-shear stress boundary condition, (3.5), at the free surface to find an expression for C_2 ;

$$\begin{aligned} C_1 [(\lambda^2 - \lambda) \cos \lambda \theta - (\lambda^2 - 3\lambda + 2) \cos(\lambda - 2)\theta] \\ + C_2 [(\lambda^2 - \lambda) \sin \lambda \theta - (\lambda^2 - \lambda) \sin(\lambda - 2)\theta] = 0, \\ C_2 = -\frac{\lambda \cos \lambda \theta - (\lambda - 2) \cos(\lambda - 2)\theta}{(\sin \lambda \theta - \sin(\lambda - 2)\theta) \lambda} C_1. \end{aligned}$$

Finally, for the kinematic boundary condition, the evaporation outflow must be satisfied at the free surface,

$$\begin{aligned} \left. \frac{\partial \psi}{\partial \rho} \right|_{\phi=\theta} &= A(\theta) U \rho^{\lambda-1}, \\ C_1 \left[\cos \lambda \theta - \cos(\lambda - 2)\theta + \frac{C_2}{C_1} \left(\sin \lambda \theta - \frac{\lambda}{\lambda - 2} \sin(\lambda - 2)\theta \right) \right] &= -\frac{A(\theta) U}{\lambda}, \\ C_1 = \frac{A(\theta) U}{2} \frac{(\lambda - 2) (\sin \lambda \theta - \sin(\lambda - 2)\theta)}{\lambda \cos \lambda \theta \sin(\lambda - 2)\theta - (\lambda - 2) \cos(\lambda - 2)\theta \sin \lambda \theta}. \end{aligned} \quad (3.14)$$

For the cases $\lambda = 1$ or 2 , different coefficients are found. Starting of with $\lambda = 1$ ($\theta = 90^\circ$), ψ is now given by (3.10). No-slip and impermeability now give

$$C_4 = -C_2, \text{ and } C_1 = 0.$$

No-shear stress at the free surface yields

$$\begin{aligned} 2C_2 \sin \theta + 2C_3 \cos \theta &= 0, \\ C_3 &= -\tan \theta C_2. \end{aligned}$$

Finally, for the kinematic boundary condition (3.2) one finds

$$\begin{aligned} C_2 (\sin \theta - \theta \tan \theta \sin \theta - \theta \cos \theta) &= -A(\theta) U, \\ C_2 &= -A(\theta) U \frac{\cos \theta}{\theta - \sin \theta \cos \theta}. \end{aligned}$$

For the special case where $\lambda = 2$ ($\theta = 135^\circ$), (3.11) can be substituted into the boundary conditions. Again, starting with no slip and impermeability one finds

$$C_4 = -2C_2, \text{ and } C_3 = -C_1. \quad (3.15)$$

No shear stress over the free surface yields

$$\begin{aligned} C_1 \cos 2\theta + C_2 \sin 2\theta &= 0, \\ C_2 &= -\frac{1}{\tan 2\theta} C_1. \end{aligned} \quad (3.16)$$

C_1 is found from the kinematic boundary condition

$$\begin{aligned} -2\rho C_1 \left(\cos 2\theta + \frac{\sin 2\theta}{\tan 2\theta} - 1 - \frac{2\theta}{\tan 2\theta} \right) &= -A(\theta) U \rho, \\ C_1 &= 2 A(\theta) U \frac{\tan 2\theta}{2\theta - \tan 2\theta}. \end{aligned} \quad (3.17)$$

3.3 Flow due to the moving interface

For the flow due to the moving interface the kinematic condition is given by

$$-\frac{\partial \psi}{\partial \rho} \Big|_{\phi=\theta} = \alpha \rho^{\alpha-1}(\dots) = -\rho B(\theta) U. \quad (3.18)$$

hence, $\alpha = 2$.

As seen in the previous paragraph, this results in a special case of the general solution, (3.11). Since the boundaries at the substrate and the no shear stress condition at the free surface still hold for the flow due to a changing interface, the solution to coefficients C_2 , C_3 , and C_4 are given in (3.15) and (3.16). In fact, the only difference with the special case $\lambda = 2$ from the flow due to the evaporative flux is C_1 , which becomes

$$C_1 = -B(\theta) \frac{U}{2} \frac{\tan 2\theta}{2\theta - \tan 2\theta}. \quad (3.19)$$

Chapter 4

Analytical results

We will now analyze the flow properties that result from the exact solutions that we derived in the previous chapter. Remarkably, we find contact angle regimes where the flow is in opposite direction as expected which we will describe. Next, we will show that depending on the contact angle, a flow type will dominate close to the contact line. When we expand the solution of the dominant flow type for small contact angles, the exact flow field solution will simplify to the result of lubrication approximation.

4.1 Wedge flow fields

The streamlines for both the flow due to evaporation and the flow due to the moving interface are given in figure 4.1 and 4.2 respectively. The spacing between the streamlines is controlled by the magnitude of the flow velocity, a larger velocity magnitude corresponding to areas of densely packed streamlines and areas of coarsely packed streamlines corresponding to areas with a low flow velocity magnitude. Remarkably, regions are found where the flow is in the opposite direction as one might suspect. For flow induced by evaporation one could reasonably expect that the flow inside the wedge must be in the outward direction due to the outward flux. There are, however, certain contact angle regions where some flow moves in the opposite direction, towards the center of the droplet, as seen in figure 4.1 for $\theta = 130^\circ, 150^\circ$, and 160° .

In the flow field due to the evaporative flux, the effect of reversal first seen in the streamlines for $\theta = 130^\circ$. One observes streamlines that will reach the free surface and streamlines that turn away from the contact line, towards the center of the droplet, separated by a dividing line. Interestingly, the reversal in the flow field has disappeared at $\theta = 140^\circ$, but reappears at $\theta = 150^\circ$. For $\theta = 160^\circ$ one even observes multiple lines that divide the flow field into different regions where the flow changes the direction.

Similar features are observed for the flow field with the moving interface boundary condition, see figure 4.2. Since the contact angle is decreasing, the flow is expected to oriented away from the contact line, yet, for $\theta = 100^\circ, 110^\circ$, and 120° regions are seen where there exists flow towards the contact line. The line that divides the different flow regimes moves upwards to the free surface as the contact angle becomes larger.

In both figures of the streamlines in the wedge, figure 4.1 and 4.2, no scale is shown. This is because these flow solutions are self-similar, i.e.

$$\frac{u_\rho}{u_\phi} = \text{constant for constant } \phi. \quad (4.1)$$

This self-similarity originates from the general solution to the biharmonic equation (3.9). The general solution gives similar powers in ρ for both velocity components, and hence, the ρ -dependency in (4.1) drops out. Note that, in general, the superposition of the solutions, the flow field due to evaporation and the flow field due to the interface movement, will not be self-similar.

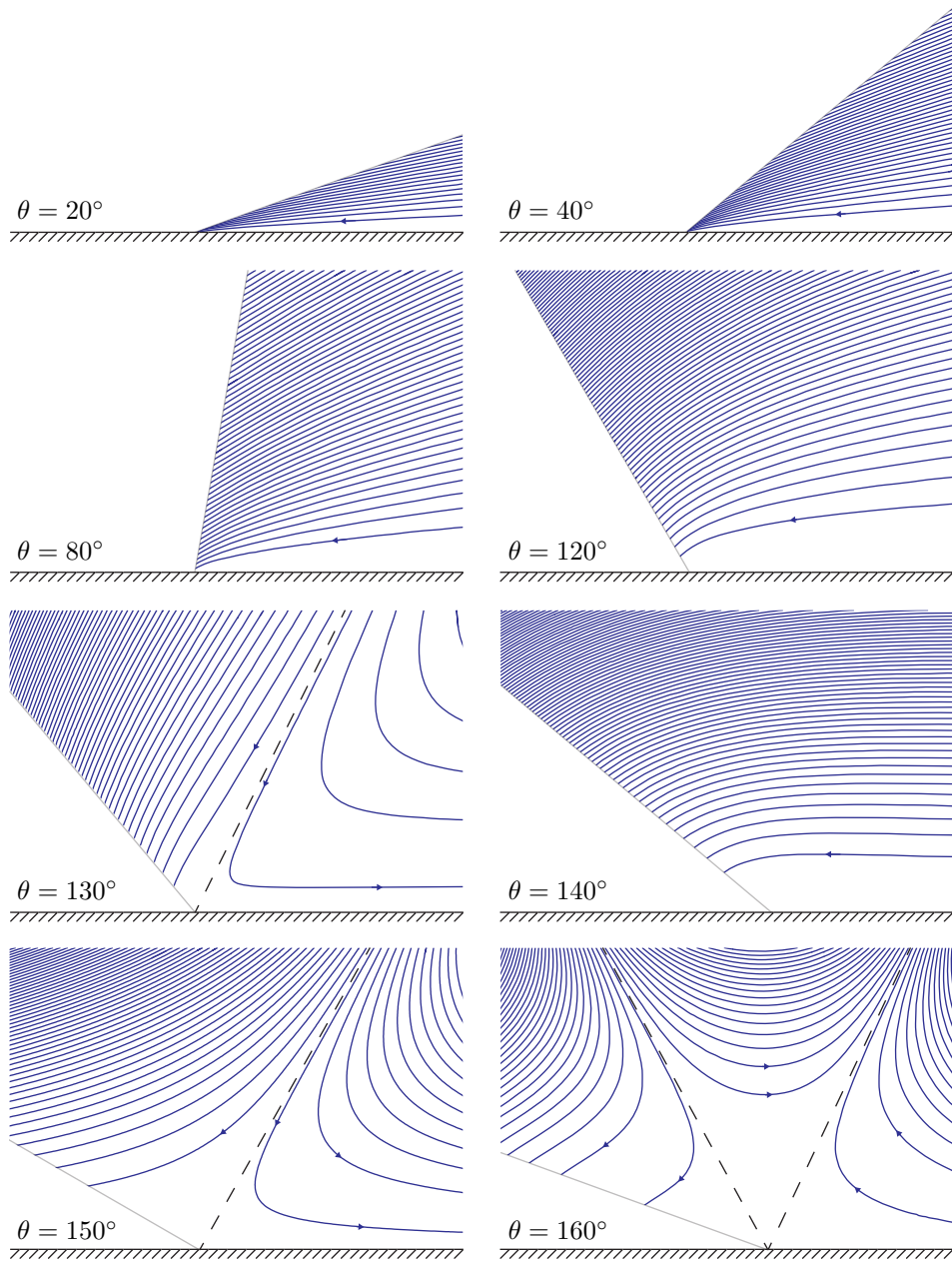


Figure 4.1: Streamlines of the flow driven by evaporation in the wedge for different contact angles. Black dashed lines mark the region where the flow changes direction.

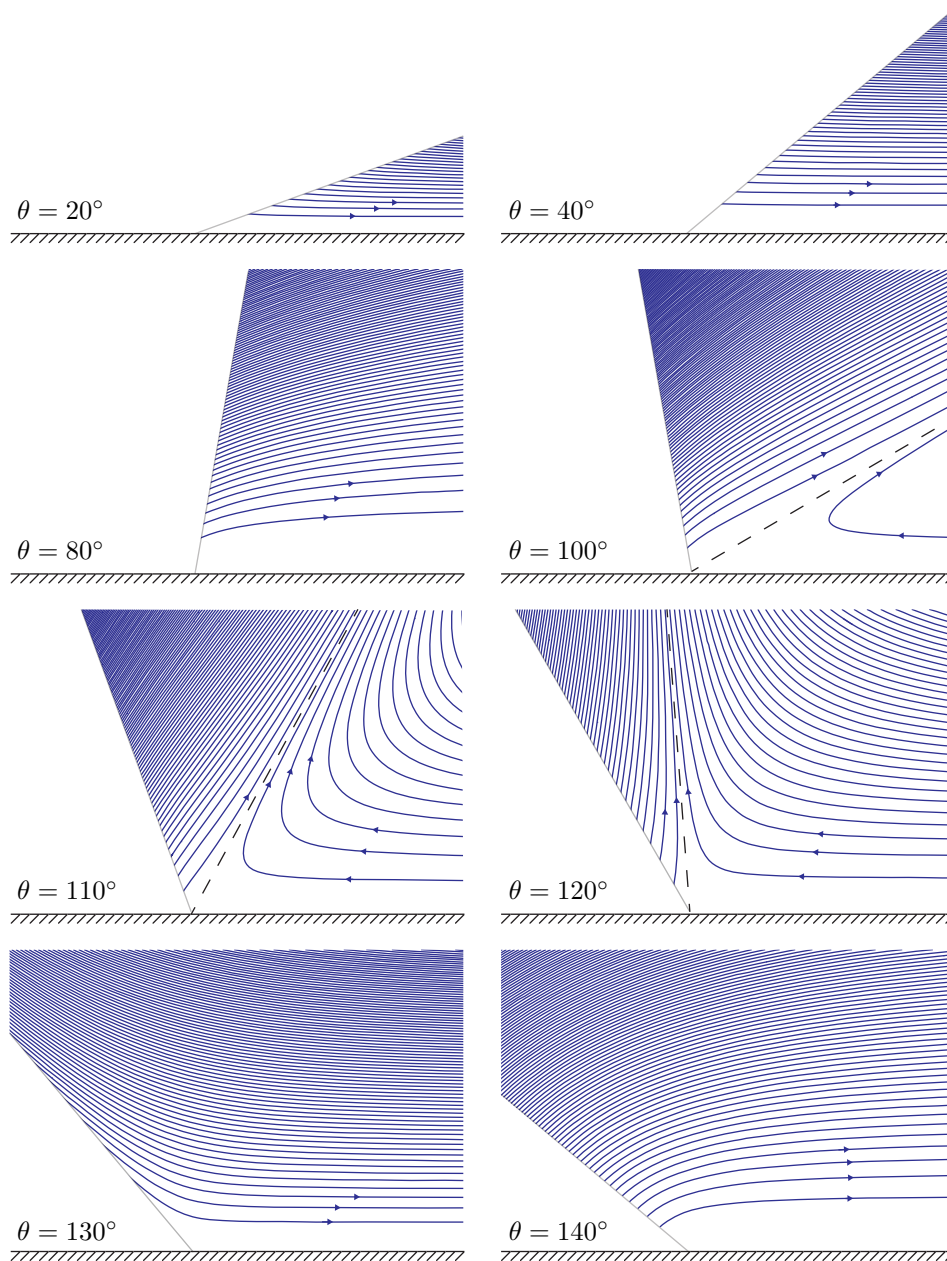


Figure 4.2: Streamlines of the flow driven by the moving interface in the wedge for different contact angles. The black dashed line marks the region where the flow changes direction.

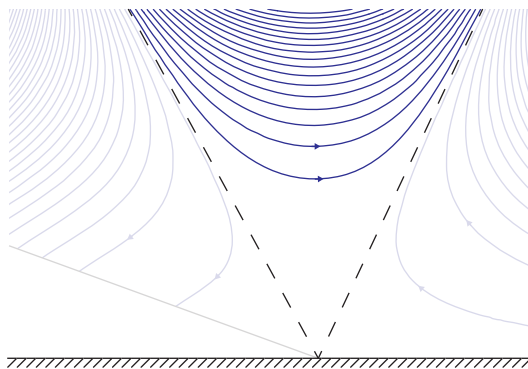


Figure 4.3: Plot of a typical flow region separated by separatrices (dashed). Streamlines are from the flow due to evaporation at a contact angle of 160° .

4.2 Regions of reversed flow

The lines that divide the flow field into the regimes where the flow changes direction are characterized by a vanishing angular velocity, the separatrices of the flow field. Here, we will try to describe the separatrices that we observe more quantitatively.

A Separatrix cannot appear suddenly inside the flow for a certain θ ; it has to enter from the boundaries. To analyze the solution at a boundary, the substrate is a convenient choice because here (3.9) simplifies. However, since the angular velocity is always zero here, which is our impermeability boundary condition, a different description for the separatrices is needed. One can demonstrate from the biharmonic equation that separatrices correspond to local extrema in the radial velocity; if we substitute that the angular velocity, and its derivatives with respect to ρ , are zero, the biharmonic equation at a separatrix gives:

$$\frac{1}{\rho^4} (\psi_{\phi\phi\phi\phi} + 4\psi_{\phi\phi}) + \frac{2}{\rho^2} \psi_{\rho\rho\phi\phi} - \frac{2}{\rho^3} \psi_{\rho\phi\phi} = 0. \quad (4.2)$$

In the first term, the derivatives of the stream function will cancel, both remaining terms now have to equal zero independently to satisfy the biharmonic equation. We find that a separatrix exists at the origin when

$$\left. \frac{\partial u_\rho}{\partial \phi} \right|_{\phi=0} = \left. \frac{1}{\rho} \frac{\partial^2 \psi}{\partial \phi^2} \right|_{\phi=0} = 0. \quad (4.3)$$

4.2.1 Separatrices in the flow due to evaporation

If (4.3) is solved for the flow due to evaporation at the substrate we find

$$\left. \frac{1}{\rho} \frac{\partial^2 \psi}{\partial \phi^2} \right|_{\phi=0} = C_1 ((\lambda - 2)^2 - \lambda^2) = 0 \text{ with } \lambda \neq 0, 1, 2. \quad (4.4)$$

Hence, a separatrix appears at the substrate if the numerator of C_1 , (3.14), is zero, i.e.

$$f(\theta) = \sin \lambda \theta - \sin(\lambda - 2)\theta = 0. \quad (4.5)$$

A plot of this function is given in figure 4.4. The zeros of this function predict the contact angles when a separatrix appears at $\phi = 0$.

The equation gives two conditions;

$$\lambda \theta + 2\pi n = \lambda \theta - 2\theta, \text{ and} \quad (4.6)$$

$$2\lambda \theta - 2\theta = \pi(2n + 1), \quad (4.7)$$

where n is an integer. The first condition gives $\theta = \pi n$ which will not result in any separatrix in the range θ from 0 to π . Hence, the the second equation for θ gives the contact angles at which a separatrix is at the substrate

$$\theta = \frac{\pi}{2} \left(\sqrt{n^2 + 2n - 1} + 1 - n \right). \quad (4.8)$$

From observing the solution of the flow in the wedge, we see that the first separatrix indeed enters the wedge at $\theta = \pi/2\sqrt{2}$ ($\theta \simeq 127^\circ$), as predicted by (4.8). For larger contact angles, the separatrix moves upwards, towards the free surface, until it disappears at the free surface. When the separatrix coincides with the free surface, there will be a conflict between the kinematic boundary condition, the outflow due to evaporation, and the separatrix, which imposes that there must be zero outflow. We observe that the separatrix leaves around 133.4° , where a division by zero in C_1 prevents us from calculating the solution.

We have derived a formula that gives us the contact angles at which a separatrix is present at the substrate. From there, we observed that the separatrix at the substrate moved upwards, into the flow field, and left the flow field at the free surface. For larger contact angles, λ will grow rapidly and more and more separatrices will be present in the flow field, making observation cumbersome. In the limit of large contact angles, however, we can approximate the angular velocity and give an estimate for the amount of separatrices in the flow field. In the limit of large λ we have,

$$C_4 = -\frac{\lambda}{\lambda - 2} C_2 \approx -C_2, \quad (4.9)$$

and, by substituting this approximation and (3.13), we can write the angular velocity as

$$\begin{aligned} u_\phi = -\frac{\partial\psi}{\partial\rho} &\approx -\lambda\rho^{\lambda-1} (C_1[\cos\lambda\theta - \cos(\lambda-2)\theta] + C_2(\sin\lambda\theta - \sin(\lambda-2)\theta)) \\ &= -\lambda\rho^{\lambda-1} \sin\phi [C_1 \sin(\lambda-1)\phi + C_2 \cos(\lambda-1)\phi]. \end{aligned} \quad (4.10)$$

The coefficients C_1 and C_2 are independent of ϕ , and the separatrices are given by zero angular velocity. Hence, the angular frequency at which reversal occurs within the wedge is estimated by

$$\lambda - 1, \quad (4.11)$$

which can be used to approximate the amount of separatrices in the wedge for large contact angles. Using the full angular domain from $\phi = 0$ to θ , we find

$$m = \left\lfloor (\lambda - 1) \frac{\theta}{\pi} \right\rfloor, \quad (4.12)$$

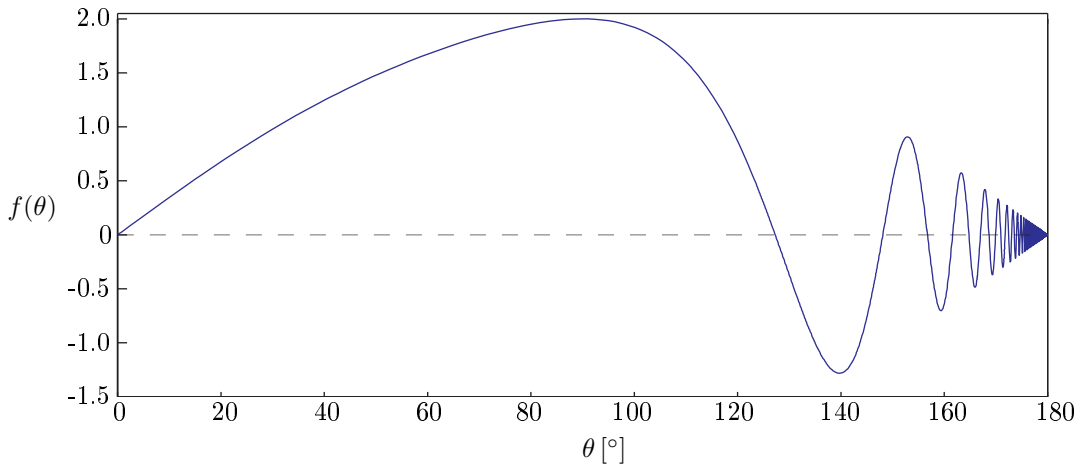


Figure 4.4: Plot of (4.5) versus the contact angle. Separatrices enter the flow field when the function passes through the horizontal axis.

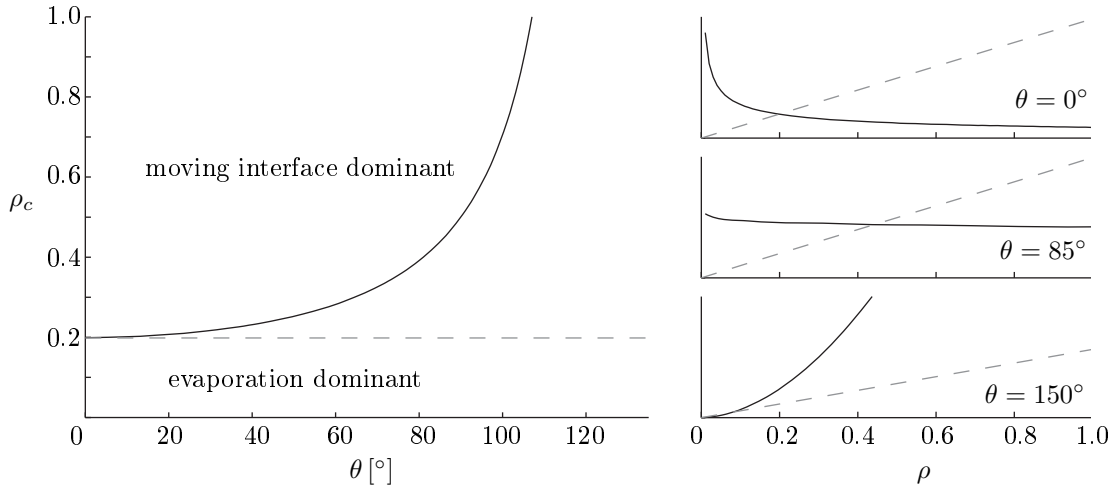


Figure 4.5: On the left side, the crossover length-scale (4.15) is plotted against different contact angles (solid black). The dashed gray line is the approximation of ρ_c for small contact angles, $\rho_c = 2^{-7/3}$. On the right side a comparison of the absolute flow normal at the free surface due to evaporation (solid black line) and moving interface (dashed gray) versus distance for different contact angles.

where m is the amount of separatrices in the wedge and the brackets note rounding to the largest previous integer.

4.2.2 Separatrices in the flow due to the moving interface

We noticed that a separatrix also appeared in the flow due to the moving interface, see figure 4.2 for contact angles $\theta = 100^\circ$, 110° , and 120° . When solving (4.3) for the stream function that describes the flow due to the moving interface one finds

$$\left. \frac{1}{\rho} \frac{\partial^2 \psi}{\partial \phi^2} \right|_{\phi=0} = -4C_1 = 0, \quad (4.13)$$

where C_1 is given in (3.19). Hence, here a separatrix appears at the substrate when

$$\sin 2\theta = 0, \quad (4.14)$$

which corresponds to $\theta = 90^\circ$ in the domain from $\theta = 0^\circ$ to 180° . Again, the separatrix moves upwards in the flow field for larger contact angles, and disappears at the free surface. We see that in C_1 a division by zero occurs around $\theta = 122.46^\circ$, which, we observe, corresponds to the separatrix leaving the flow field.

4.3 Dominant flow driving mechanism

As discussed in section 3.1, there are two mechanisms that drive the flow inside the wedge: the evaporative flux and the moving interface. Because of the different powers of ρ in these mechanisms, one will, in general, be stronger than the other for certain ρ , see figure 4.5. A crossover length-scale can be defined at which the dominating driving mechanism for the flow changes. This crossover length-scale can be found by equating the right hand side of (3.6) to zero;

$$A(\theta) U \rho_c^{\lambda-1} - B(\theta) U \rho_c = 0,$$

where ρ_c is in dimensionless form, see (2.3). The crossover length-scale is found as

$$\rho_c = \left(\frac{B(\theta)}{A(\theta)} \right)^{1/(\lambda(\theta)-2)}. \quad (4.15)$$

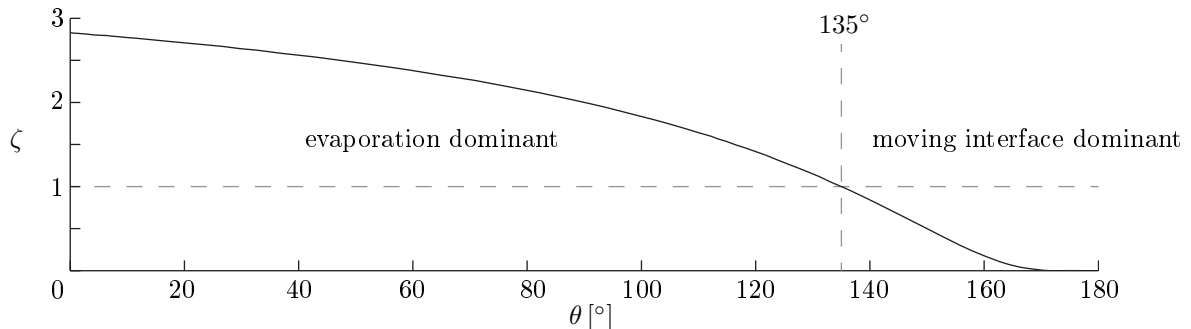


Figure 4.6: Plot of the velocity ratio (4.16) versus contact angle at $\rho = 1/2\rho_c$. It can be seen that evaporation is the dominant flow driving mechanism for $0 < \rho < \rho_c$ when $\theta < 135^\circ$, for $\theta > 135^\circ$ the changing interface will be the main driving force.

For contact angles smaller than 135° ($\lambda = 2$), the flow due to evaporation is dominant below the crossover length scale due to the negative power in ρ . However, above 135° degrees the hinge flow is dominant in the region $\rho < \rho_c$. This can be shown by comparing both flows

$$\zeta = \frac{u_\phi^{evap}}{u_\phi^{hinge}} = \frac{A(\theta)}{B(\theta)}\rho^{\lambda(\theta)-2}. \quad (4.16)$$

where u_ϕ^{evap} is the angular velocity of the flow due to evaporation at the free surface, u_ϕ^{hinge} the angular velocity of the flow due to the moving interface at the free surface, and ζ the ratio between these flow driving mechanisms. If this number is larger than one for given ρ , evaporation is the dominant flow driving mechanism. Otherwise, for a ratio smaller than one, the hinge movement is the driving mechanism, see figure 4.6. It should be noted that $A(\theta)/B(\theta)$ is of order unity, and it can be seen that a crossover takes place at $\lambda = 2$.

In the limit of small contact angles, the functions $A(\theta)$, $B(\theta)$, and λ become independent of θ and are given by (2.14), (2.20), and $\lambda = 1/2$. Here we find a crossover length of a fifth of the droplet radius, and thus, evaporation is dominant close to the contact line for small contact angles, see figure 4.5.¹

4.4 Towards the lubrication approximation

To verify the validity of the lubrication approximation close to the contact line, we expand the Stokes flow solution in the limit of small θ and ϕ . In this limit the flow due to evaporation is dominant and the flow field is approximated by neglecting contribution of the flow due to the moving interface. A Laurent series is used to expand the solution around $\theta = 0$ to include θ of negative degree [23],

$$\psi = A(\theta)U\sqrt{\rho}\left(8\sin^3\frac{1}{2}\phi\theta^{-3} - 3\left(\cos\frac{3}{2}\phi - \cos\frac{1}{2}\phi\right)\theta^{-2} - 5\sin^3\frac{1}{2}\phi\theta^{-1}\right) + O(\theta^0),$$

whereupon a Maclaurin series is used to expand the solution for ϕ ,

$$\psi = A(\theta)U\sqrt{\rho}\left[-3\left(\frac{\phi}{\theta}\right)^2 + \left(\frac{\phi}{\theta}\right)^3 - \frac{5\phi^3}{8\theta}\right] + O(\theta^3).$$

The terms ϕ/θ are of order unity, whereas the last term will be of order θ^2 . In the small contact angle limit this last term is negligible, as well as other higher order terms, and an approximation

¹The dominant effect of the evaporative flux over the moving interface close to the contact line for small contact angles also appeared in section 2.2.1, (2.31). Here we saw that the contribution due to the moving interface can be neglected because of the higher power in ρ .

of the flow field is found,

$$\psi \approx A(\theta) U \sqrt{\rho} \left[-3 \left(\frac{\phi}{\theta} \right)^2 + \left(\frac{\phi}{\theta} \right)^3 \right]. \quad (4.17)$$

When looking at small contact angles, the Cartesian coordinates can be approximated from the polar coordinates as

$$x = R \rho \cos \phi \approx R \rho \quad y = R \rho \sin \phi \approx R \rho \phi, \text{ and } h \approx R \rho \theta, \quad (4.18)$$

and we can write,

$$\frac{\phi}{\theta} \approx \frac{z}{h}. \quad (4.19)$$

Hence, the horizontal velocity component can be obtained from (4.17) as, using (2.14) for the flux constant,

$$u_r \approx -\frac{1}{\rho} \frac{\partial \psi}{\partial \phi} \approx -\frac{6\sqrt{2} U R}{\pi h} \sqrt{\rho} \left[\frac{1}{2} \left(\frac{z}{h} \right)^2 - \left(\frac{z}{h} \right) \right]. \quad (4.20)$$

Which is exactly similar to the result obtained by applying the lubrication approximation, given in (2.33), section 2.2.2, providing a solid mathematical argument for applying the lubrication theory to describe the flow in evaporating droplets in the limit of small contact angles. In figure 4.7 the lubrication approximation is plotted together with the exact solution for different θ . For convenience, the velocities are scaled to the velocity at the free surface. One can see good agreement, even up to relatively large contact angles.

One could have expected this result from the streamlines of the flow due to evaporation in figure 4.1 for contact angles 20° and 40° , which look remarkably similar to the flow field obtained by the lubrication approximation in figure 2.4. In contrast to the argument of Hu & Larson, the streamlines arrive more tangential than normal at the free surface.

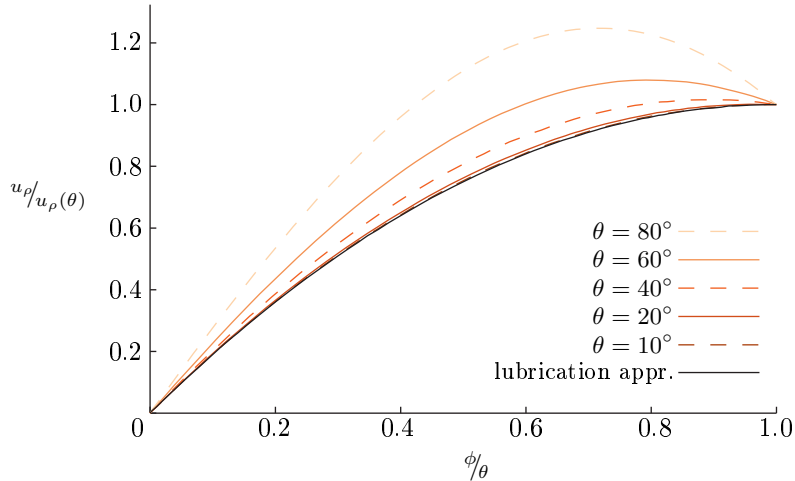


Figure 4.7: Lubrication approximation plotted against the exact radial velocity normalized by the velocity at the free surface for different θ .

4.4.1 Why the lubrication theory works

From the presented results it is clear that even close to the contact line, where the evaporative flux is diverging, the lubrication approximation can be applied. Instead of the mathematical argument a, perhaps, more intuitive method can be tried to explain the validity of the lubrication approximation close to the contact line.

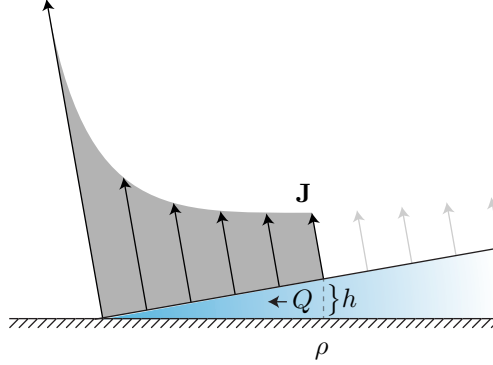


Figure 4.8: Illustration to estimate the velocity components at ρ . The flux \mathbf{J} gives the approximately vertical mass flow at the free surface. The horizontal flux through the wedge of height h , Q , is given by the total outflow from ρ to the contact line, which is marked by the shaded area.

If the argument of Hu & Larson [17] in section 2.2.2 is recalled, at small contact angles and close to the contact line, the vertical velocity at the free surface can be approximated as,

$$u_z|_{z=h} \approx u_\phi|_{\phi=\theta} = \frac{\sqrt{2}}{\pi} \frac{U}{\sqrt{\rho}}. \quad (4.21)$$

Now instead of abandoning the lubrication approximation due to the singular velocity, we will look for an estimate of the horizontal velocity. This component is estimated by the amount of fluid passing through the wedge at given ρ . The flow close to the contact line is evaporation driven, thus the flux through the wedge at given ρ is given by the amount of fluid that evaporates in the domain from ρ to the contact line,

$$\frac{Q(\rho)}{\rho_l} = \int_0^\rho \frac{\sqrt{2}}{\pi} \frac{U}{\sqrt{\rho'}} d\rho' = \frac{\sqrt{2}}{\pi} U \sqrt{\rho}, \quad (4.22)$$

see figure 4.8. This flow has to squeeze itself through the local height of the wedge, approximately $\theta \cdot \rho$. Now the height average velocity, which is the average horizontal velocity, is given by,

$$\bar{u}_r \approx -\frac{Q(\rho)}{\rho_l \theta \rho} = -\frac{\sqrt{2}}{\pi} \frac{U}{\theta \sqrt{\rho}}. \quad (4.23)$$

and the ratio between the velocities becomes,

$$\frac{u_r}{u_z} \propto \frac{1}{\theta}. \quad (4.24)$$

We see that even though the vertical velocity is singular around the origin, the horizontal velocity possesses the same singularity, but in addition is also inversely proportional to the contact angle. For small contact angles, the horizontal flow will be much larger than the vertical velocity, resulting in an approximate horizontal velocity. This is contradictory to the argument of Hu & Larson and implies that the lubrication approximation may indeed be used to describe the flow for small contact angles.

Chapter 5

Wedge flow simulation

For the numerical simulations COMSOL¹ will be used. COMSOL is chosen for the ability to easily couple different physics problems together in the simulation; here the concentration field outside of the droplet and flow field inside the droplet. In this chapter we will validate the COMSOL code by comparing numerical solutions for the wedge with the analytical solutions described in chapter 3.

5.1 Wedge model description

To validate the numerical code we want to solve a case which we can verify with the analytical wedge solution. We analytically solved the concentration field and evaporative flux, as described in section 2.1, and the flow field in chapter 3. Here, we will numerically solve the wedge-flow problem for $\theta = 40^\circ$ and compare it with the analytical solution, a case with $\theta = 130^\circ$ is solved to observe if the regions of reversed flow are seen in the numerical simulation. In the simulation, again, the Laplace equation will be solved to find the concentration field,

$$\nabla^2 c = 0. \quad (5.1)$$

For the flow inside the droplet, however, the continuity for incompressible fluids and Stokes equation are solved directly,

$$\nabla \cdot \mathbf{u} = 0, \text{ and} \quad (5.2)$$

$$\mu \nabla^2 \mathbf{u} = \nabla p, \quad (5.3)$$

where p is the pressure, instead of via the stream function.

The analytical solutions for the wedge are self-similar and extend all the way to infinity. For the numerical simulation, however, the physical domain has to be bounded at certain $\rho = P$ and boundary conditions must be applied to these newly introduced boundaries, see figure 5.1. For reference purposes we will call these newly introduced boundaries the “far-field boundaries”.

The far-field boundaries impose problems for the comparison of the results obtained by numerical simulation and the analytical results. One could substitute the analytical solution on the boundaries, but then the influence of these boundaries on the solution of the numerical simulation is unknown. Therefore, we impose different boundary conditions here and compare the numerical solution with the analytical solution close to the contact line.

For the concentration field we specify the same boundary conditions as in section 2.1, but in addition we introduce a boundary condition at the vapor far-field boundary,

$$c|_{\rho=P} = \cos \lambda(\phi - \theta), \quad (5.4)$$

where λ is given in (3.7). Instead of introducing a constant $c = 0$ at the boundary, which will result in a singularity in the evaporative flux at the far-field, this boundary condition will introduce a

¹COMSOL MULTIPHYSICS®, version 4.2.1.110.

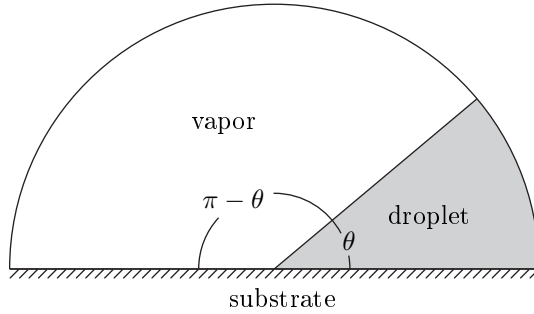


Figure 5.1: Geometry of the wedge flow problem used for the validation case. The arcs that close the wedge containing the vapor concentration and the wedge containing the fluid are newly introduced compared to the analytic case and are referred to as the far-field boundaries.

small normal derivative, and thus, a small flux. For $\theta < 90^\circ$ this is justified, whereas for $\theta > 90^\circ$ this boundary condition will introduce large errors. For the case with $\theta = 130^\circ$ we want a boundary condition that will give a larger flux at the free surface, instead of (5.4), we chose

$$c|_{\rho=P} = 1 - \sin \lambda(\phi - \theta), \quad (5.5)$$

which is derived from the analytical solution, (2.10), at $\rho = 1$.

At the far-field boundary for the fluid a condition is wanted that does not directly affect the flow; here we chose a fixed pressure,

$$p|_{\rho=P} = p_0. \quad (5.6)$$

Next to the no-slip (3.3), impermeability (3.4) and the no shear-stress (3.5) boundary conditions, we will only include the evaporative flux condition at the free surface, and neglect the moving interface condition because of its dominance for cases where $\theta < 135^\circ$. Hence, at the free surface we impose,

$$u_\phi|_{\phi=\theta} = \frac{J}{\rho l} = -\frac{D}{\rho l} \mathbf{n} \cdot \nabla c. \quad (5.7)$$

5.2 Set-up in COMSOL

The equations for the concentration field and flow field are implemented as presented above with the specified boundary conditions. The concentration field and flow field will be solved sequentially, starting with the concentration field because of the dependency of the evaporative flux on the concentration field, to save computational resources.

Near the contact line, a dense mesh is needed to capture the high gradients in c , \mathbf{u} , and p . The mesh generation algorithms in COMSOL do not cope well with large variations in cell sizes and a custom-made mesh is generated. Because the geometry consists of two circular segments, an algorithm is created to build a mesh for a circular segment with a dense nodal distribution near the contact line, see figure 5.2 (a). The mesh is built mainly out of arcs of quadrilateral elements that follow the ϕ coordinate. As the quadrilateral elements come closer to the contact line, their size decreases, resulting in a denser mesh until a critical distance ρ_m after which triangular elements are introduced to break-down the arc of quadrilateral elements and converge towards the corner, see figure 5.2 (b). In the break down region, quadrilateral elements are still used where they result in better aspect ratios than triangular elements.

To solve the problem we use the MUMPS solver for the concentration field and PARDISO for the flow field. The tolerance factor in COMSOL is set to 1 to as convergence criteria.

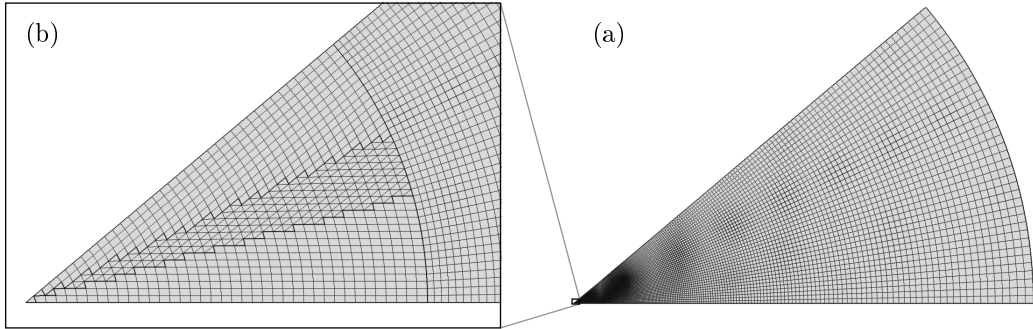


Figure 5.2: (a) The generated mesh for a circular segment. The black lines display cell boundaries, the node points are positioned at the intersections of the black lines. Inset (b) shows a magnification of the mesh close to the origin.

5.3 Results for $\theta = 40^\circ$

A numerical simulation is performed for the case with $\theta = 40^\circ$. The quadrilateral arcs are generated at 1° ϕ -intervals and extend from $\rho = 1$ to 10^{-6} . The total mesh consists out of 160.150 elements (triangular and quadrilateral).

First we will analyze the exterior problem by comparing the evaporative flux of the numerical simulation with the analytical solution given in (2.12). The correct-power law behavior of the numerical solution is shown in figure 5.3 (a). Here the evaporative flux of the simulation is plotted together with the analytic solution. The analytic solution includes a prefactor $A(\theta)$ to fit the local wedge solution to the solution of the entire droplet. In the simulation this link to the entire droplet is missing and a different prefactor is expected. In order to compare the two solutions, the factor $A(\theta)$ is chosen to fit the result of the numerical simulation. Near $\rho = 1$ a different behavior due to the far-field boundary is seen, but the evaporative flux converges rapidly to the analytic power-law and good agreement is seen over a large amount of decades. Even as ρ goes to zero, the singularity is described well by the numerical solution.

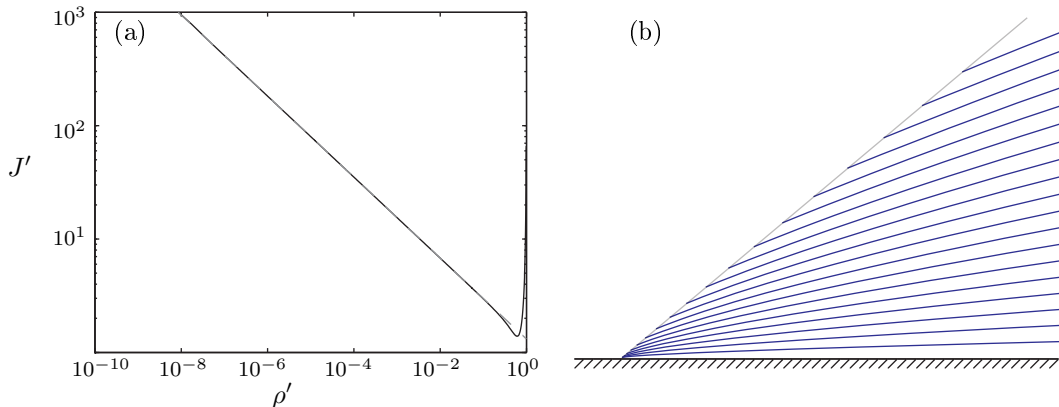


Figure 5.3: (a) Comparison of the evaporative flux of the numerical simulation (solid black) and the analytical solution (dashed gray) for $\theta = 40^\circ$. The factor $A(\theta)$ in the analytic solution is fitted to the numerical solution. (b) Streamlines of the numerical simulation in the wedge for $\theta = 40^\circ$, close to the origin.

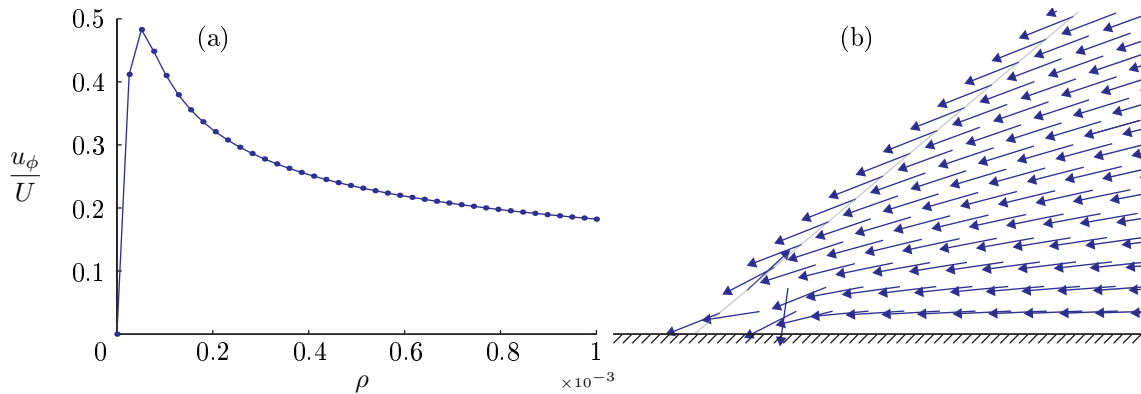


Figure 5.4: (a) Outflow at the free surface, close to the contact line. The node points are marked and connected linearly. (b) Arrows of the flow direction, the invalid behavior near the origin can be clearly seen.

The evaporative flux drives a flow in the wedge; a plot of the streamlines of this flow is created using the numerical solution on the domain $\rho = 0$ to 10^{-3} , and is shown in figure 5.3 (b). The result appears to be in good agreement with the streamlines of the analytic solution, shown in figure 4.1. Near the contact line, between $\rho = 0$ and ρ_m , the numerical solution deviates from the analytical solution. Here, a conflict in boundary conditions at the contact line results in an invalid outflow as can be seen in figure 5.4 (a). The no-slip and impermeability boundary conditions dominate over the outflow boundary condition. This results in an invalid outflow for the node at the origin and the adjacent node on the free surface, giving rise to an incorrect flow field near the origin, as can be seen in figure 5.4 (b).

A more quantitative validation of the numerical simulation can be made by calculating how much the numerical solution deviates from the analytical solution. In figure 5.5 (a) the angle of the flow (ϕ -direction), the direction of the streamlines with respect to the substrate, of the numerical solution is compared with the analytic solution at all node points with $\rho < 10^{-1}$. Again, it can be seen that close to the origin, the numerical solution differs ($0 - 1^\circ$ at ρ_m) from the analytic solution. In figure 5.5 (b) the absolute velocity at the node points is compared with the analytic solution. Similar as done for comparison of the evaporative flux, the factor $A(\theta)$ is missing and the numerical solution is fitted to the analytic solution in the region $10^{-4} < \rho < 10^{-2}$. The flow magnitude of the simulation is lower than the analytic result near the origin. This can be explained by the missing outflow at the first two node points, see figure 5.4 (a). Yet, we find an excellent agreement of the numerical solution with the analytical solution in a range ρ from 10^{-4} to 10^{-1} .

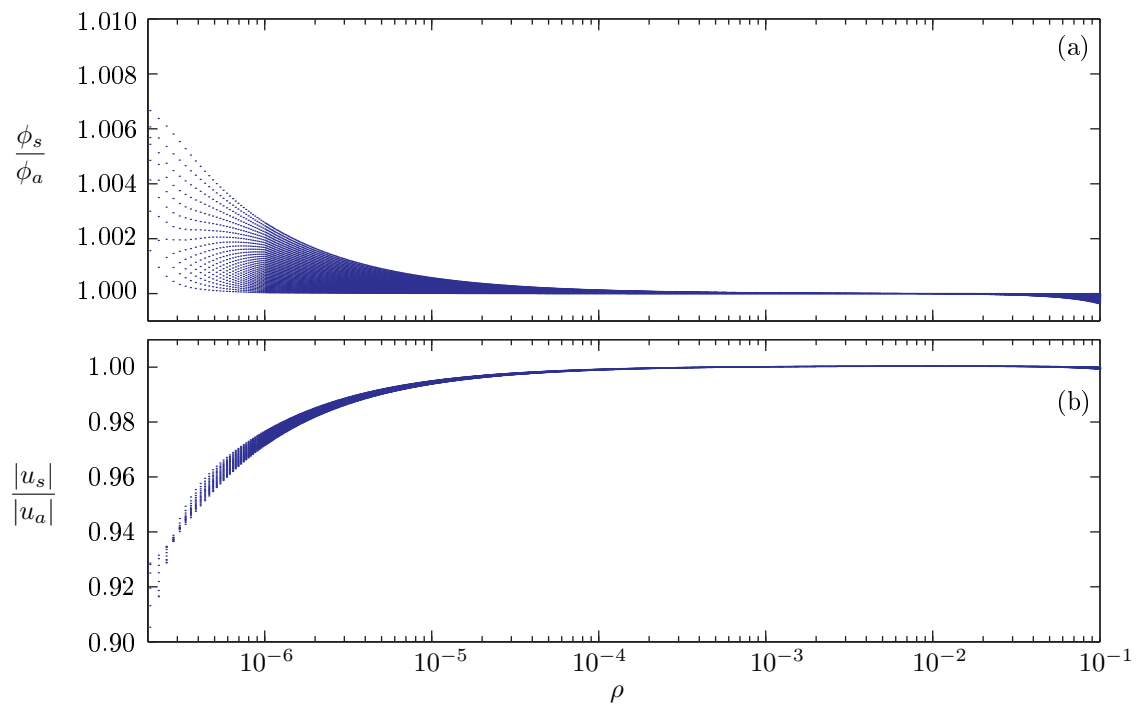


Figure 5.5: Comparison of the numerical solution for the flow field for a wedge (subscript s) and the analytic solution (subscript a) for $\theta = 40^\circ$. (a) Comparison of the direction of the flow with respect to the substrate versus distance. (b) Comparison of the velocity magnitude.

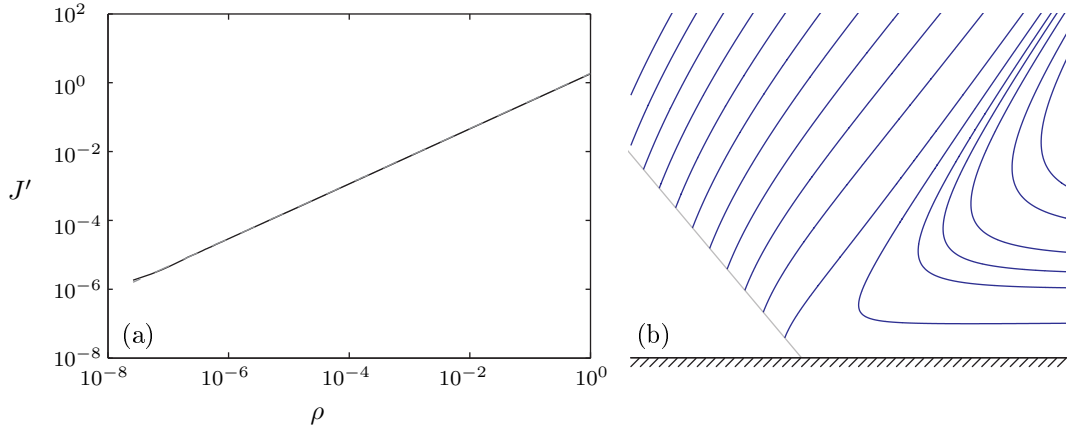


Figure 5.6: (a) The evaporative flux of the simulation (solid black) and the evaporative flux of the analytical solution (dashed gray) versus radial distance. (b) Streamlines near the origin, $0 \leq \rho \leq \rho_m$.

5.4 Results for $\theta = 130^\circ$

The reason for performing numerical simulations was investigation of the separatrices, which is why a case is created for $\theta = 130^\circ$, where a separatrix appeared in the analytical solution to the flow field due to evaporation, see figure 4.1. The mesh of this case, again, consists of arcs of quadrilateral elements which are by 1° , only this time ρ_m is set to 10^{-5} . The total mesh consists of 120.707 elements.

The evaporative flux, again, shows good agreement with the analytical solution after fitting of $A(\theta)$, see figure 5.6 (a). The streamlines, figure 5.6 (b), promisingly show a region of reversed flow. The far-field boundary condition of constant pressure is not compatible with the flow reversal, and the self-similarity is lost. If streamlines are plotted from the region $0 \leq \rho \leq 10^{-1}$, it becomes apparent that the region of reversed flow, from the numerical simulation, corresponds to a circulation inside the wedge, see figure 5.7. This confirms that the small-scale flow reversal is very robust, and seems to be unavoidable. For a closed geometry, as in the entire droplet, one therefore expects circulation as clearly visible in figure 5.7.

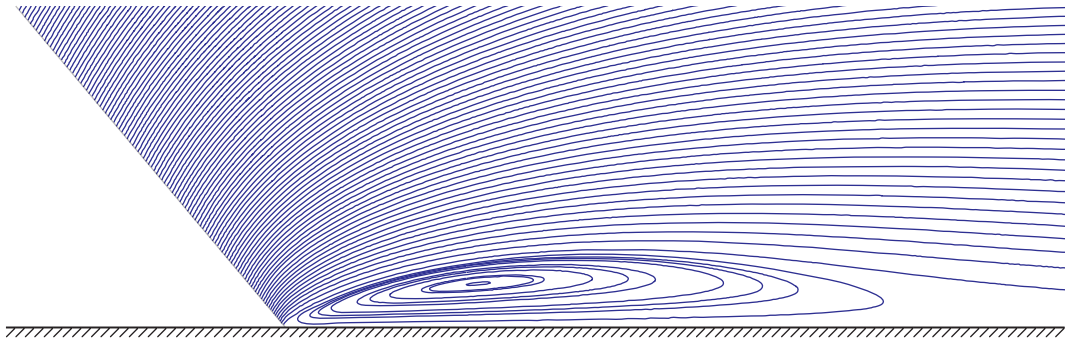


Figure 5.7: Streamlines of the flow field from the numerical simulation for $\theta = 130^\circ$ revealing a circulation inside the wedge, radial distance $0 \leq \rho \leq 10^{-1}$.

Chapter 6

Numerical results

In this chapter we will present the results of numerical simulations for the whole droplet geometry. First, differences with the validation case will be discussed after which we will compare the evaporative flux with analytical Popov solutions [10]. To close off, we will make a small comparison of the flow field and the wedge and show some more results of the circulation seen inside the droplet.

6.1 Droplet model description

The model to solve the flow in the whole droplet is set-up in a similar way as the validation case for the wedge in chapter 5. Here, the geometry of the droplet is confined by itself and no artificial boundaries have to be introduced. The concentration field, on the contrary, does have to be bounded, see figure 6.1. The problem is axisymmetric and the droplet is described by a perfect spherical cap, see figure 6.1.

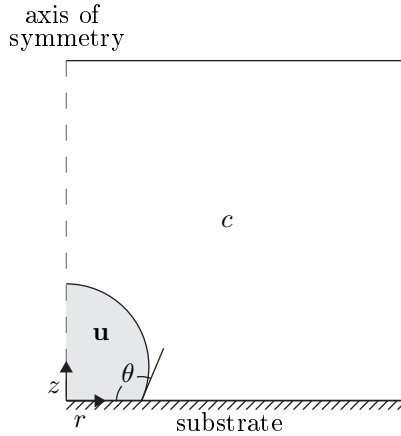


Figure 6.1: Illustration of the geometry used for the numerical simulation of the evaporating droplet of contact angle θ (gray), together with cylindrical coordinates r and z . The dashed line shows the axis of symmetry. The top and most right lines mark the far-field boundaries.

The far-field boundary condition for the concentration field is placed far away from the droplet, such that the vapor concentration can be approximated to be the vapor concentration at infinity,

$$c = 0 \text{ in the far-field.} \quad (6.1)$$

On the free surface of the droplet, the vapor concentration is saturated and we impose

$$c = 1 \text{ at the free surface.} \quad (6.2)$$

At the substrate and symmetry axis there is a zero-flux condition for the concentration field,

$$\frac{\partial c}{\partial z} = 0 \text{ at } z = 0 \text{ and } r = 0. \quad (6.3)$$

The boundary conditions for the droplet are more complex than for the fluid wedge because the droplet is a closed geometry. In the wedge case we could impose the evaporative flux on the free surface and the far-field boundary would allow for replenishment of the fluid that evaporates. In the closed geometry of the droplet, this replenishing of the fluid is taken care of by the shrinkage of the droplet. To satisfy continuity, the total outflow of the droplet must be compensated by an inward flow due to the movement of the boundary, quite similar to how the time derivative of the contact angle was found in section 2.1.2. The total outflow can be calculated from the surface integral of the evaporative flux,

$$\frac{dM}{dt} = \int_S J dS, \quad (6.4)$$

where S is the free surface area. This outflow due to evaporation combined with the mass of a spherical cap [10],

$$M = \rho_l \pi R^3 \frac{\cos^3 \theta - 3 \cos \theta + 2}{3 \sin^3 \theta} \quad (6.5)$$

yields a time derivative of the contact angle θ ,

$$\frac{d\theta}{dt} = \frac{d\theta}{dM} \frac{dM}{dt} = \frac{(1 + \cos \theta)^2}{\rho_l \pi R^3} \frac{dM}{dt}. \quad (6.6)$$

Next, to find an expression for the movement of the boundary, we make use of toroidal coordinates, see figure 6.2,

$$r = R \frac{\sinh \tau}{\cosh \tau - \cos \sigma}, \text{ and} \quad (6.7)$$

$$z = R \frac{\sin \sigma}{\cosh \tau - \cos \sigma}, \quad (6.8)$$

where lines of constant σ correspond with the free surface of the droplet for different contact angles, $\sigma = \pi - \theta$, and the τ coordinate is normal to the free surface. Hence, using (6.6), the boundary movement can be expressed as;

$$u = \sqrt{\left(\frac{\partial r}{\partial \theta}\right)^2 + \left(\frac{\partial z}{\partial \theta}\right)^2} \frac{d\theta}{dt} = \frac{1}{\rho_l \pi R^2} \frac{(1 + \cos \theta)^2}{\cosh \tau + \cos \theta} \frac{dM}{dt}, \quad (6.9)$$

and is normal to the free surface.

Finally, the kinematic boundary condition at the free surface is given by the sum of the outflow due to the evaporative flux, (5.7), and the moving boundary, (6.9),

$$u = -\frac{D}{\rho_l} \left(\mathbf{n} \cdot \nabla c - \frac{1}{\pi R^2} \frac{(1 + \cos \theta)^2}{\cosh \tau + \cos \theta} \int_S \mathbf{n} \cdot \nabla c dS \right). \quad (6.10)$$

Note that this boundary condition is similar to (3.6) used for the analytical solution, where also an outflow due to the evaporative flux and an inward flow due to the moving boundary. The other boundaries remain similar; at the free surface no-shear stress is imposed, at the substrate no-slip and impermeability,

$$\mathbf{u} = 0 \text{ at } z = 0, \quad (6.11)$$

and axial symmetry at the axis of revolution,

$$\frac{\partial \mathbf{u}}{\partial r} = \mathbf{0} \text{ at } r = 0. \quad (6.12)$$

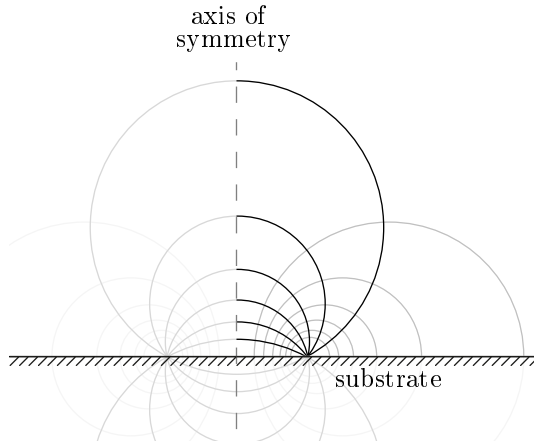


Figure 6.2: Illustration of the toroidal coordinate system. The lines of constant σ follow the free surface of the droplet for different contact angles and are displayed as solid black. The lines of constant τ are gray.

6.2 Results

To present results on the free surface, we introduce a length ℓ which compares the arc-length from the position on the free surface to the contact line with the total arc length of the free surface from the contact line towards the axis of symmetry,

$$\ell = \frac{1}{\theta} \arctan \frac{z - z_o}{r} - \frac{1}{2} \frac{\pi}{\theta} + 1, \quad (6.13)$$

where

$$z_o = -R \tan \left(\frac{1}{2} \pi - \theta \right), \quad (6.14)$$

is the vertical offset to the center of the droplet, see figure 6.3. The length maps the contact line at zero and increases to one at the top of the droplet, the axis of symmetry, see figure 6.3.

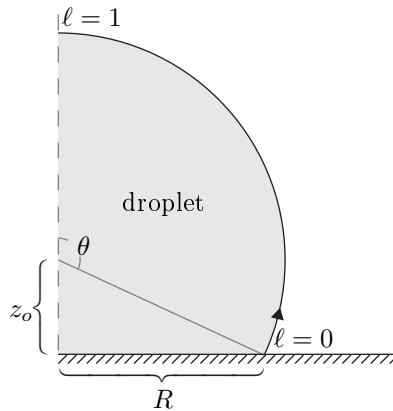


Figure 6.3: Illustration of the length on the free surface, (6.13). $\ell = 0$ coincides with the contact line and $\ell = 1$ with the axis of symmetry.

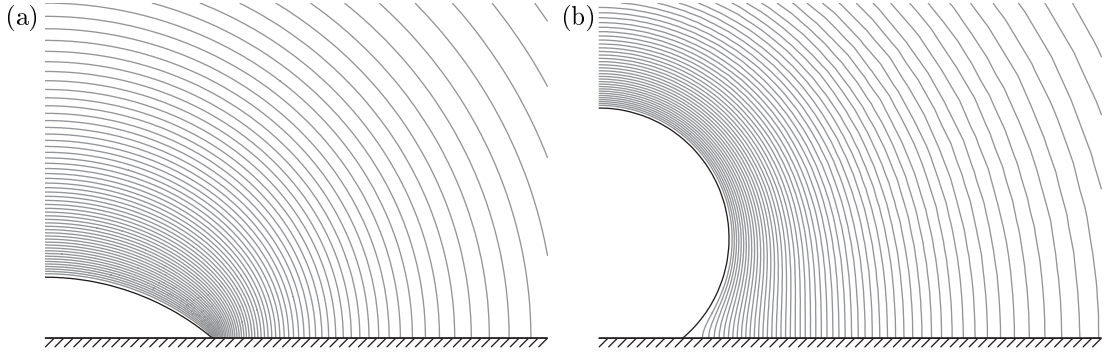


Figure 6.4: Contour plots of the concentration field outside of the droplet for (a) $\theta = 40^\circ$ and (b) $\theta = 140^\circ$ obtained from the numerical simulation.

6.2.1 Concentration field and evaporative flux

Contour plots of the concentration for droplet with contact angles of 40° and 140° are shown in figure 6.4. Regions with closely packed contour lines mark the areas with large evaporation. The difference between the negative and positive power in the evaporative flux is clearly seen; for the case with $\theta = 40^\circ$, figure 6.4 (a), the contours are packed closely at the contact line, where the singular evaporative flux is found. In the second case, $\theta = 140^\circ$, the contours are sparse around the origin and, the evaporation is suppressed, as we have seen in section 2.1.

The analytical solution of Popov [10] is derived for an unbounded geometry, and showed good agreement with experiments [11]. For the simulations, the far-field boundaries had to be introduced. To investigate the effect of these boundaries, a comparison with the analytical solutions of Popov is shown in figure 6.5 for the cases with $\theta = 40^\circ$ and 140° . We see good agreement with the solutions of Popov without adjustable parameters, small deviations are only seen close to the contact line. Since ℓ provides us with a length scale that goes linearly with ρ close to the contact line, the evaporative fluxes are displayed on log scales to show that the power-law close to the contact line. In figure 6.5 it is shown that a power-law is in agreement with the numerical simulations for the whole droplet and the analytical solutions from Popov.

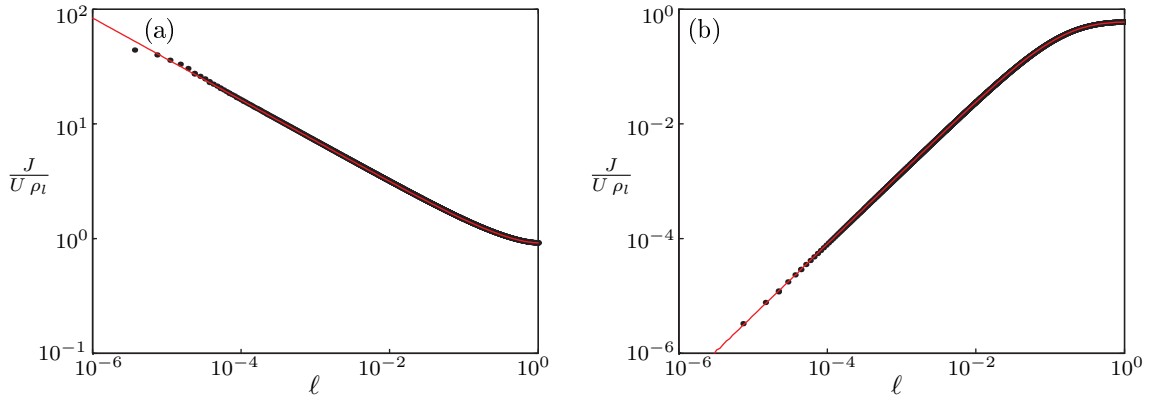


Figure 6.5: Comparison of evaporative flux found from the numerical simulation (black dots) and the analytical solution of Popov [10] (red line) versus ℓ for (a) $\theta = 40^\circ$ and (b) 140° . The black dots correspond to the node positions of the mesh.

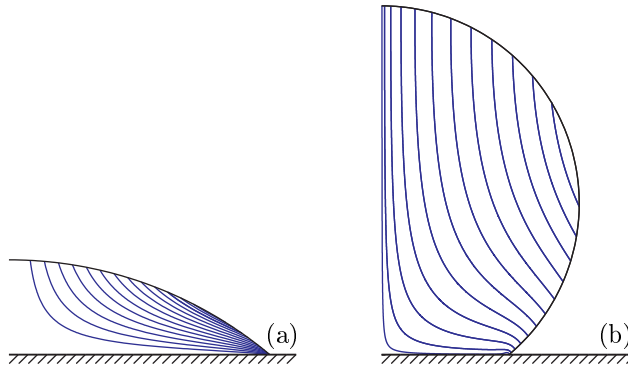


Figure 6.6: Streamlines in the droplet for (a) $\theta = 40^\circ$ and (b) 140° . Note that the position of these streamlines does not indicate the velocity magnitude but only the direction of the flow field.

6.2.2 Droplet flow fields

The evaporative flux from the preceding section drives a flow inside the droplet, shown in figure 6.6. Even though the streamlines for both cases look convincing, the validation case for $\theta = 40^\circ$ revealed that problems may occur near the contact line due to the singular evaporative flux. Indeed, a similar break down in the solution is seen for the simulation of the whole droplet, see figure 6.7.

Contrary to the validation case, here, due to the break-down of the solution the continuity equation is no longer satisfied. The actual outflow due to evaporation is not similar to the imposed evaporative flux from the exterior problem near the contact line, see figure 6.7 (b). Since there is less outflow than predicted from the exterior problem, the boundary movement overcompensates the outflow due to evaporation and a non-zero net mass flux trough the free surface appears. Scaling this net flux gives an estimate for an error in the simulation,

$$e = \frac{\cos \theta + 1}{2\pi R^2} \frac{1}{U} \int_S \mathbf{n} \cdot \mathbf{u} dS, \quad (6.15)$$

which is of order 10^{-4} for this case while typical values of other simulations of large contact angles, $\theta = 130^\circ, 140^\circ,$ and $150^\circ,$ are of order 10^{-12} .

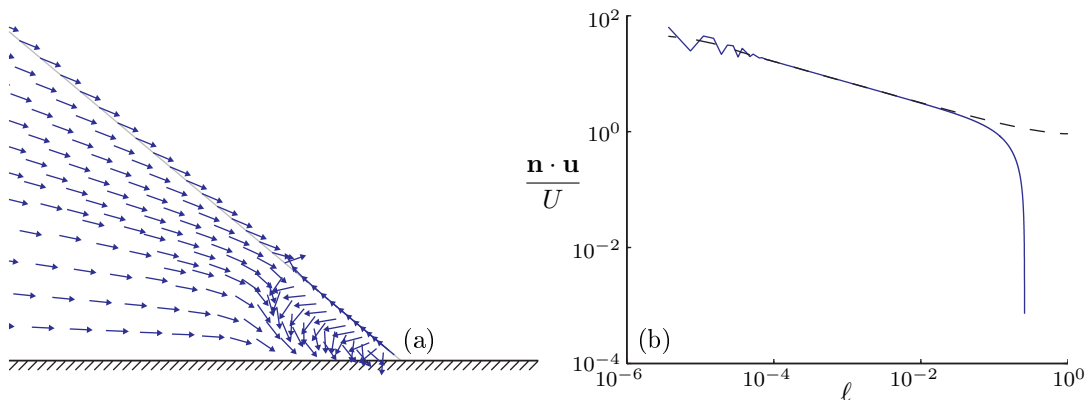


Figure 6.7: Breakdown of the flow field in the corner of the droplet for $\theta = 40^\circ$. (a) shows the direction of the flow at the mesh nodes. (b) Comparison of the imposed outflow due to the evaporative flux (dashed black) and the actual outflow in the simulation (blue). Flow due to evaporation is dominating close to the contact line.

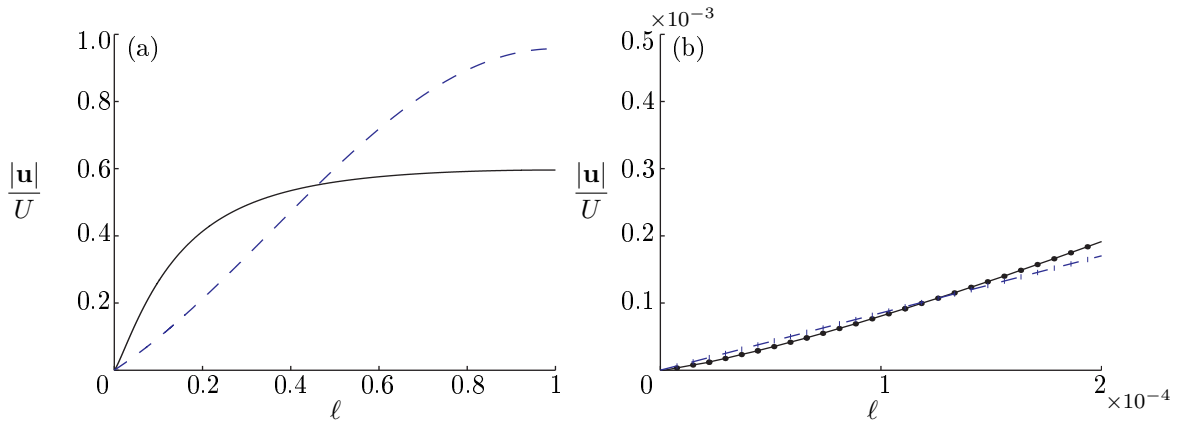


Figure 6.8: (a) Comparison of the different flow driving mechanisms, in black the outflow due to evaporation and in dashed blue the inward flow due to the boundary movement, scaled by the velocity U over the free surface. (b) The same data, but close to the contact line. Here it can be seen that the flow due to the moving boundary dominates, as predicted in section 4.3. The dots correspond with node points of the mesh.

Close to the contact for the case where $\theta = 140^\circ$ also shows interesting behavior. We derived in section 4.3 that here the movement of the boundary is dominant over outflow due to evaporation close to the contact line. In figure 6.8 (a) and (b) the magnitudes of the different flow driving mechanisms are compared and one can indeed see that in the numerical simulation the moving boundary is dominant near the contact line, see figure 6.8 (b). When moving further over the free surface, away from the contact line towards the center of the droplet, the evaporative flux will dominate over the boundary movement which is again overtaken by the moving boundary about half-way on the free surface. Close to the contact line there is a flow towards the center of the droplet. Hence, to create outflow further away from the contact line, a circulation must exist inside the droplet, as seen in figure 6.9.

A small dent is seen in the circulation near the contact line. Observation of this dent revealed that it originated from a circulation enclosing solely the node point at the contact line and the first node point from the contact line further among the free surface. This could indicate that the dent seen in the larger circulation is an artifact of the numerical simulation. Indeed, when a local refinement is made in the mesh close to the contact line, the dent decreases in size and again it solely seems to depend on the first two node points of the mesh. In figure 6.9 the streamlines of both the coarse and locally refined case are shown to observe the grid independence of the results.

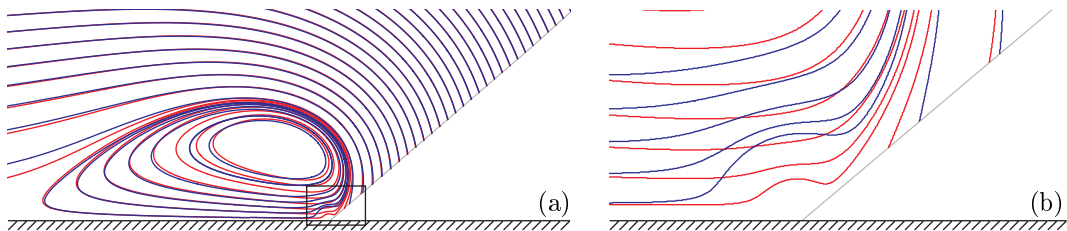


Figure 6.9: (a) Streamlines near the corner of a droplet with contact angle of 140° . (b) A close-up of the streamlines local around the contact line, showing an artifact of the simulations. In blue, streamlines of a coarser mesh (total of 96293 elements) are shown together with streamlines at the same location of a locally refined mesh (total of 108579 elements) in red. The streamlines of both solutions are generated in COMSOL and pass through the same line.

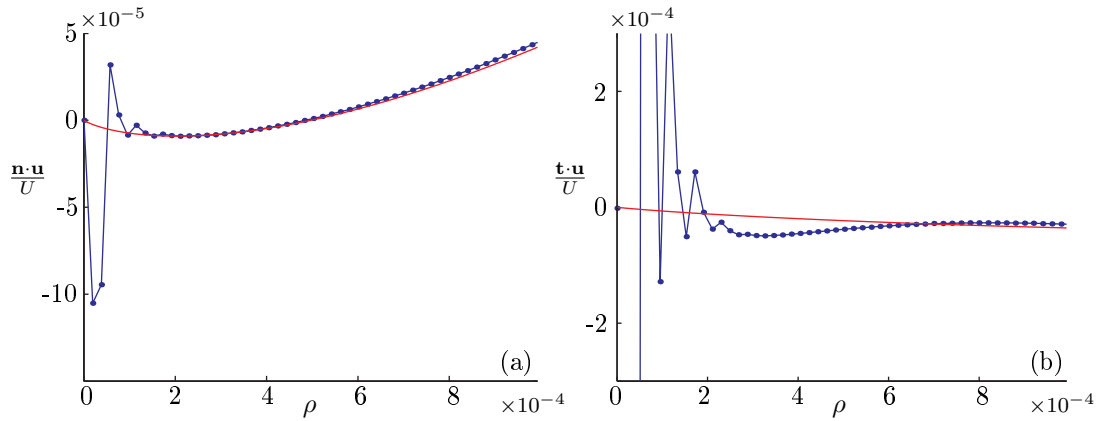


Figure 6.10: Comparison of the flow near the contact line for numerical simulation of the droplet (blue, dots at the node points) and the analytical wedge solution (red) in (a) the normal direction and (b) the tangential direction with respect to the free surface. For the droplet geometry, ρ is the dimensionless distance to the contact line.

More investigation can be done on the dent in the streamlines; the normal velocity and tangential velocities can be compared to the analytical solution in the wedge, see figure 6.10. Divergence near the contact line can be seen in the simulation, especially in figure 6.10 (b) where the tangential component is presented. The alternating tangential velocity for adjacent node points near the contact line hint at a numerical error that damps with for increasing distance from the contact line. A small note on the figure, the factors $A(\theta)$ and $B(\theta)$ used in the analytical solution are not fitted as was necessary for the validation case but are derived from the small ρ limit of the solutions from Popov [10]. Away from the contact line, one can see good agreement for the normal flow simulated in the droplet compared to the analytical wedge solution up to a ρ of order 10^{-3} . Streamlines of the analytical solution also show the larger circulation we found in the simulation, see figure 6.11.

The circulation seen for $\theta = 140^\circ$ cannot appear at once in the wedge, but will have to grow for increasing θ . In figure 6.12 (a) the streamlines of the numerical simulation of a droplet with $\theta = 130^\circ$ are plotted. For contact angles close to 135° , the driving mechanisms are equally important and a superposition of the flow fields of both driving mechanisms is shown in figure 6.12 (b), where we see a separatrix. We expect that this separatrix bounds the area of circulation in the entire droplet, as illustrated in figure 6.12. Even though the solution of the numerical simulation does not behave well close to the contact line, the circulation appears to be bounded by the separatrix.

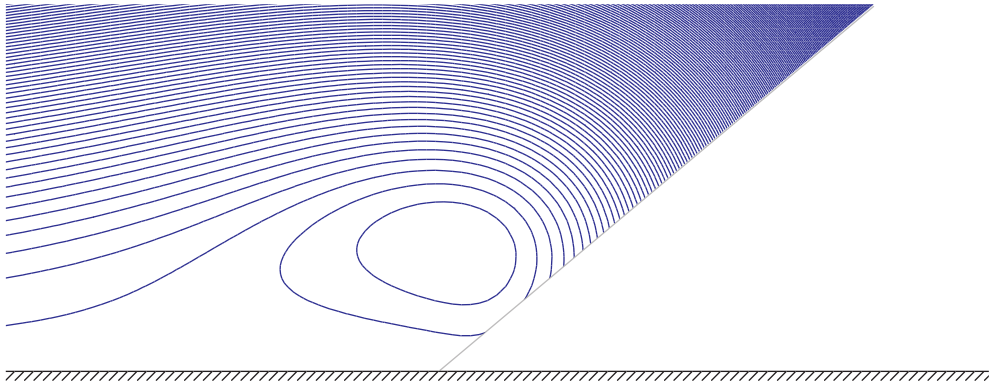


Figure 6.11: Streamlines for the analytical wedge solution, using a superposition of the solution due to the evaporative flux and the solution due to the moving boundary, with $\theta = 140^\circ$.

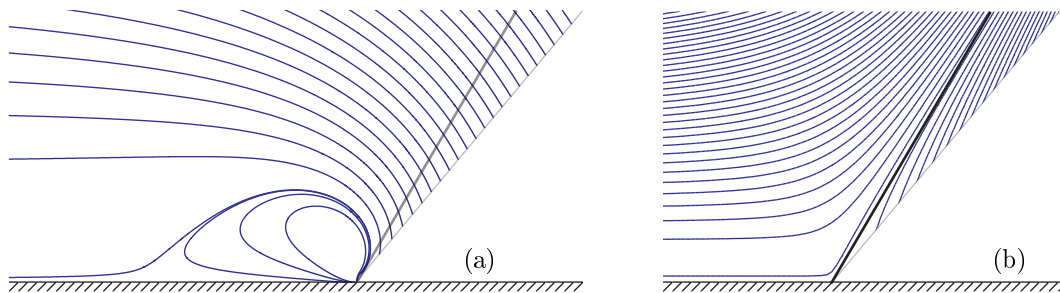


Figure 6.12: Streamlines near the corner for the numerical simulation of the entire droplet with $\theta = 130^\circ$ (a) and the total analytical wedge solution, superposition of both flow driving mechanisms (b). A line with the same angle as the separatrix in the analytical case overlain in (a).

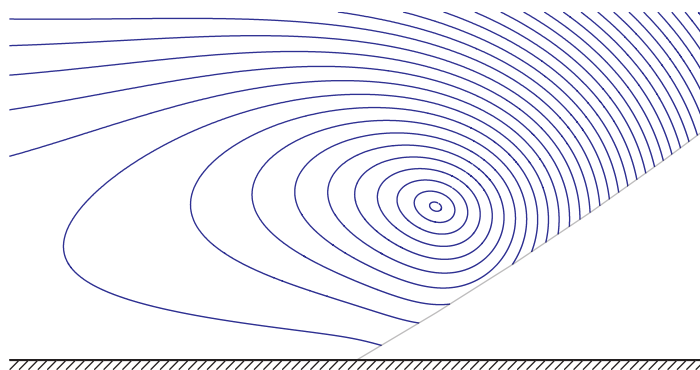


Figure 6.13: Streamlines near the corner of a droplet with a contact angle of 150° on a domain of $-0.2 \times R$ to $0.2 \times R$.

For larger contact angles the flow due to the moving interface dominates more and more over the flow due to the evaporative flux near the contact line. More flow inwards close to the contact line is expected to give a larger circulation, and indeed, if the streamlines for a droplet with $\theta = 150^\circ$ are plotted the circulation becomes visible at a larger scale, see figure 6.13.

Chapter 7

Discussion and conclusion

In this final chapter we briefly reflect and summarize the work that we have done, closing off with several suggestions for future research on evaporating droplets.

7.1 Conclusion

In this work we analytically solved the Stokes equations in the vicinity of the contact line, where the geometry simplifies to that of a wedge, for an arbitrary contact angle. We found that two driving mechanisms for the flow exist: the outwards evaporative flux from the surface of the droplet and the downwards motion of the liquid-air interface. In the contact angle region with $\theta < 135^\circ$ the evaporative flux is the dominant flow driving mechanism close to the contact line, above 135° the motion of the interface is dominant.

We demonstrated that expansion of the exact solution for small contact angles gives a solution identical to the solution obtained by application of the lubrication approximation. Hence, the lubrication approximation accurately describes the velocity field in droplets, of small contact angle, close to the contact line. Indeed, we see that the streamlines are not directed normal to the free surface as was hypothesized by Hu & Larson [17], but arrive at a well defined angle, almost parallel to the substrate. Another physical argument for this, next to the expansion of the stream function that we have derived, was given from a mass balance close to the contact line. The horizontal mass flux for droplets of small contact angle has to be squeezed through an area with a small height. This results in the same singularity in both velocity components, but giving the horizontal component a prefactor that is inversely proportional to the contact angle. Hence, for small contact angle the horizontal velocity is much larger than the vertical velocity.

The analytical solution of the flow field near the contact line also allowed us the opportunity to investigate the flow field for larger contact angles. Remarkably, for larger contact angles regions exist where the flow is in the opposite direction as one might expect; i.e. when there is an outflow at the free surface, one would expect the flow to be directed towards the free surface. However, we found regions where the fluid moves towards the center of the droplet. These regions are bounded by separatrices which we describe analytically.

To study these regions of reversed flow in more detail, numerical simulations were performed for the entire droplet geometry. In these simulations a circulation in the droplet is indeed seen in the region predicted by the analytical solution. We numerically investigated the flow fields for the entire droplet of contact angles $\theta = 130^\circ$, 140° , and 150° , for which circulation is observed. We observe that the circulation becomes larger as the flow due to evaporation becomes less important compared to the flow due to the moving liquid-air interface close to the contact line. More work is needed to further quantify the comparison between the numerical simulations and the analytical solutions.

7.2 Discussion and recommendations for future research

An advantage of the analytical solution is that we can cope with the singularity in the evaporative flux. For contact angles below 90° we saw errors in the numerical simulations close to the origin due to the singularity in the evaporative flux. However, the numerical results obtained for the exterior problem, solving the concentration field and finding the evaporative flux, are in good agreement with the analytical solutions of Popov [10] up to $\rho = 10^{-8}$. From this exterior problem, one could extract the prefactors $A(\theta)$ and $B(\theta)$ which we used in the analytical solution of the wedge problem to fit the flow field due to evaporation and the flow field due to the moving boundary to the solution of the whole droplet. We therefore propose that in the future, the problematic region close to the contact line can be replaced with the analytical solution of the wedge, resulting in a well defined problem that COMSOL can solve.

The singular evaporative flux gives rise to a singular velocity field in the analytical solution. The question that remains is what physical mechanism is responsible for the regularization of this singularity. In attempt to regularize this singularity within the limits of continuum mechanics, we tried to couple the concentration field at the free surface with the diverging pressure field using the Kelvin equation, see also [24]. The Kelvin equation relates the liquid pressure to the saturated vapor concentration. The huge pressure at the contact line will give rise to a very low saturated vapor concentration. Despite the singularity in the pressure field, the prefactors that couple the pressure to the vapor concentration prevented the coupling to be of any physical meaning. Influence on the concentration field was seen in the nanometer range, well below the mean free path of the water molecules. Perhaps the regularization could occur on the length scale of the mean free path, where continuum mechanics fail. This remains an important issue for future investigation.

Another effect that could be taken into account is that the nonuniform evaporative flux gives rise to a local cooling of the droplet [5]. The resulting temperature gradients alter the surface tension locally, thereby driving a flow over the free surface. Throughout this work this Marangoni flow is neglected as the effect is not seen in experiments with water droplets [25]. Other fluids, however, do show the Marangoni flow and inclusion of this flow in the numerical model could be of interest. The temperature field in the droplet can be solved while coupled to both the flow field and evaporative flux. When this temperature field is known, the Marangoni flow can be calculated and incorporated in the boundary condition at the free surface.

More research on the circulation that we observed in the droplet can be done. Perhaps a critical τ_c could be found to express the length where the dominant mechanism changes, likewise to the critical ρ_c that we found for the wedge. This critical distance will give the position of the stagnation point from the circulation at the free surface, and thereby can provide a rough description of the circulation inside the droplet. We imagine that visualization of this circulation in experiments will be cumbersome due to the large contact angles at which the circulation occurs, the small size and velocity of the circulation, and influence of the substrate roughness and tracer particles.

Acknowledgments

This thesis would not have been possible without the efforts of my supervisors, Hanneke Gelderblom and Jacco Snoeijer. I would like to express my gratitude to both of them for the valuable discussions that helped me tremendously throughout the graduation, and their seemingly never-ending enthusiasm for the project, in prosperity and adversity of the research. A special thanks to the fellow students of Meander room 236, Gerben Morsink, Roeland van der Veen, Nikolai Oudalov, Matthias van de Raa, and Erwin van der Poel, for their ideas, input, and, most of all, because of the joy they brought to the office. I would like to thank my girlfriend, Mirte Lohuis, family, and friends, for their indefatigable support which helped me through the harder times of graduation. I thank Prof. Dr. Detlef Lohse for giving me the opportunity to graduate in the Physics of Fluids group.

Bibliography

- [1] Á. Marín, H. Gelderblom, D. Lohse, and J. H. Snoeijer. Order-to-Disorder Transition in Ring-Shaped Colloidal Stains. *Phys. Rev. Lett.*, 107(8):1–4, August 2011.
- [2] K. P. Velikov, C. G. Christova, R. P. A. Dullens, and A. van Blaaderen. Layer-by-layer growth of binary colloidal crystals. *Science*, 296(5565):106–9, April 2002.
- [3] E. R. Dufresne, E. I. Corwin, N. A. Greenblatt, J. Ashmore, D. Y. Wang, A. D. Dinsmore, J. X. Cheng, X. S. Xie, J. W. Hutchinson, and D. A. Weitz. Flow and Fracture in Drying Nanoparticle Suspensions. *Phys. Rev. Lett.*, 91(22):1–4, November 2003.
- [4] T. P. Bigioni, X. Lin, T. T. Nguyen, E. I. Corwin, T. A. Witten, and H. M. Jaeger. Kinetically driven self assembly of highly ordered nanoparticle monolayers. *Nature Mater.*, 5(4):265–70, April 2006.
- [5] R. D. Deegan, O. Bakajin, and T. F. Dupont. Capillary flow as the cause of ring stains from dried liquid drops. *Nature*, 389(6653):827–829, 1997.
- [6] P. J. Yunker, T. Still, M. A. Lohr, and A. G. Yodh. Suppression of the coffee-ring effect by shape-dependent capillary interactions. *Nature*, 476(7360):308–311, August 2011.
- [7] H. B. Eral, D. Mampallil Augustine, M. H. G. Duits, and F. Mugele. Suppressing the coffee stain effect: how to control colloidal self-assembly in evaporating drops using electrowetting. *Soft Matter*, 7(10):4954, 2011.
- [8] J. Jing, J. Reed, J. Huang, X. Hu, V. Clarke, J. Edington, D. Housman, T. S. Anantharaman, E. J. Huff, B. Mishra, B. Porter, A. Shenker, E. Wolfson, C. Hiort, R. Kantor, C. Aston, and D. C. Schwartz. Automated high resolution optical mapping using arrayed, fluid-fixed DNA molecules. *Proc. Nat. Acad. Sci.*, 95(14):8046–51, July 1998.
- [9] R. D. Deegan. Pattern formation in drying drops. *Phys. Rev. E*, 61(1):475–85, January 2000.
- [10] Y. Popov. Evaporative deposition patterns: Spatial dimensions of the deposit. *Phys. Rev. E*, 71(3):1–17, March 2005.
- [11] H. Gelderblom, Á. Marín, H. Nair, A. van Houselt, L. Lefferts, J. H. Snoeijer, and D. Lohse. How water droplets evaporate on a superhydrophobic substrate. *Phys. Rev. E*, 83(2):1–6, February 2011.
- [12] R. D. Deegan, O. Bakajin, T. F. Dupont, G. Huber, S. R. Nagel, and T. A. Witten. Contact line deposits in an evaporating drop. *Phys. Rev. E*, 62(1 Pt B):756–65, July 2000.
- [13] B. J. Fischer. Particle Convection in an Evaporating Colloidal Droplet. *Langmuir*, 18(1): 60–67, January 2002.
- [14] H. Masoud and J. D. Felske. Analytical solution for Stokes flow inside an evaporating sessile drop: Spherical and cylindrical cap shapes. *Phys. Fluids*, 21(4):042102, 2009.

- [15] A. J. Petsi and V. N. Burganos. Stokes flow inside an evaporating liquid line for any contact angle. *Phys. Rev. E*, 78(3):1–9, September 2008.
- [16] H. Hu and R. G. Larson. Evaporation of a sessile droplet on a substrate. *J. Phys. Chem. B*, 106(6):1334–1344, 2002.
- [17] H. Hu and R. G. Larson. Analysis of the Microfluid Flow in an Evaporating Sessile Droplet. *Langmuir*, 21(3-2):3963–3971, September 2005.
- [18] A. Cazabat and G. Guéna. Evaporation of macroscopic sessile droplets. *Soft Matter*, 6(12):2591, 2010.
- [19] J. Polking, A. Boggess, and D. Arnold. *Differential Equations with Boundary Value Problems*. Prentice Hall, 2nd edition, 2006. ISBN 9780131862364.
- [20] A. Oron, S. H. Davis, and S. G. Bankoff. Long-scale evolution of thin liquid films. *Rev. Mod. Phys.*, 69(3):931–980, 1997.
- [21] J. H. Michell. On the direct determination of stress in an elastic solid, with application to the theory of plates. *Proc. London Math.*, i:100–124, 1899.
- [22] H. K. Moffatt. Viscous and resistive eddies near a sharp corner. *Fluid Mech.*, 18, March 1964.
- [23] E. B. Saff and A. D. Snider. *Fundamentals of Complex Analysis*. Prentice Hall, 3 edition, 2003. ISBN 9780139078743.
- [24] J. Eggers and L. M. Pismen. Nonlocal description of evaporating drops. *Phys. Fluids*, 22(11):112101, 2010.
- [25] H. Hu and R. G. Larson. Marangoni effect reverses coffee-ring depositions. *J. Phys. Chem. B*, 110(14):7090–4, April 2006.
- [26] P. K. Kundu and I. M. Cohen. *Fluid Mechanics*. Academic Press, 4th edition, 2008. ISBN 978-0-12-373735-9.

List of Figures

1.1	A typical coffee stain.	1
1.2	Illustration of the origin of flow towards the contact line	2
1.3	The rate of mass loss of the droplet versus contact angle	2
1.4	A droplet with reflection on the substrate, showing the singular geometry	3
1.5	Impression of the streamlines according to the argument of Hu & Larson	3
1.6	Schematic representation of the wedge problem	4
2.1	Schematic presentation of the evaporative flux problem in the wedge	6
2.2	Plot of the concentration field and evaporative flux for different contact angles	8
2.3	Illustration of the mass balance of the droplet	10
2.4	The flow field obtained from the lubrication approximation	11
2.5	Impression of the streamlines according to the argument of Hu & Larson	12
3.1	Visualization of the internal flow problem	13
4.1	Streamlines of the flow due to the evaporative flux for different contact angles	18
4.2	Streamlines of the flow due to the moving interface for different contact angles	19
4.3	Typical reversed flow region	20
4.4	Plot of the substrate separatrix condition	21
4.5	Crossover length-scale versus contact angle	22
4.6	Velocity ratio versus contact angle	23
4.7	Comparison of the lubrication approximation versus the exact wedge solution	24
4.8	Illustration of the mass flow in the wedge	25
5.1	Simulation wedge flow geometry	28
5.2	Generated mesh for a circular segment	29
5.3	Comparison of the flux for $\theta = 40^\circ$	29
5.4	Flow near the origin for $\theta = 40^\circ$	30
5.5	Wedge flow field comparison for $\theta = 40^\circ$	31
5.6	Evaporative flux and streamlines for $\theta = 130^\circ$	32
5.7	Wedge circulation streamlines for $\theta = 130^\circ$, showing circulation	32
6.1	Geometry of the droplet simulation	33
6.2	Illustration of the toroidal coordinate system	35
6.3	Description of the free surface coordinate	35
6.4	Concentration fields for the whole droplet geometry	36
6.5	The evaporative flux over the free surface for $\theta = 40^\circ$ and 140°	36
6.6	Streamlines for the droplet with contact angles $\theta = 40^\circ$ and 140°	37
6.7	Breakdown of the flow field in the corner for $\theta = 40^\circ$	37
6.8	Comparison of the flow driving mechanisms for $\theta = 140^\circ$	38
6.9	Streamlines near the corner of a droplet with a contact angle of 140°	38
6.10	Comparison of the flow for the droplet and the wedge with $\theta = 140^\circ$	39
6.11	Analytical streamlines near the corner of the wedge with $\theta = 140^\circ$	39

6.12 Streamlines near the corner of a droplet with a contact angle of 130°	40
6.13 Streamlines near the corner of a droplet with a contact angle of 150°	40

Appendix A

Typical droplet properties

The typical properties of the droplet that are used throughout this thesis are taken from the supplementary material of [1] and are listed in the table below, together with derived values.

Table A.1: Droplet properties from Marín et al. [1], or otherwise when noted.

R	1×10^{-3}	m	
ρ_l	9.98×10^2	$\text{kg} \cdot \text{m}^{-3}$	
μ	1.002×10^{-3}	$\text{kg} \cdot \text{m}^{-1} \cdot \text{s}^{-1}$	[26]
D_{va}	24×10^{-6}	$\text{m}^2 \cdot \text{s}^{-1}$	
Δc	1.2×10^{-2}	$\text{kg} \cdot \text{m}^{-3}$	

Table A.2: Derived droplet values from table A.1

U	$= D_{va} \Delta c / R \rho_l$	2.9×10^{-7}	$\text{m} \cdot \text{s}^{-1}$
Re	$= D_{va} \Delta c / \mu$	2.9×10^{-4}	
Bo	$= \frac{(\rho_l - \rho_a) g R^2}{\sigma}$	1.3×10^{-1}	